A Mixed Perfectly-Matched-Layer for Transient Wave Simulations in Axisymmetric Elastic Media

S. Kucukcoban[1] and L.F. Kallivokas[2]

Abstract: We are concerned with elastic wave simulations arising in elastic, semi-infinite, heterogeneous, three-dimensional media with a vertical axis of symmetry through the coordinate origin. Specifically, we discuss the development of a new mixed displacement-stress formulation in PML-truncated axisymmetric media for forward elastic wave simulations. Typically, a perfectly-matched-layer (PML) is used to surround a truncated finite computational domain in order to attenuate outwardly propagating waves without reflections for all non-zero angles-of-incidence and frequencies. To date, standard formulations use split fields, where the displacement components are split into normal and parallel to the PML interface components. In this work, we favor unsplit schemes, primarily for the computational savings they afford when compared against split-field methods. We use complex-coordinate stretching in the frequency-domain, but retain both unsplit displacements and stresses as unknowns prior to inverting the stretched forms back into the time-domain. We use a non-classical mixed finite element approach, and an extended Newmark-β scheme to integrate in time the resulting semi-discrete forms, which in addition to the standard terms, include a jerk or jolt term. We report on numerical simulations demonstrating the stability and efficacy of the approach.

Keywords: Perfectly matched layer; transient elastodynamics; wave propagation; mixed finite elements; axisymmetric media

1   Introduction

Problems requiring the simulation of waves in unbounded domains arise commonly in many science and engineering disciplines. When domain discretization methods

---

[1] Department of Civil, Architectural and Environmental Engineering, The University of Texas at Austin, 1 University Station, C1748, TX 78712, USA

[2] Department of Civil, Architectural and Environmental Engineering, The University of Texas at Austin, 1 University Station, C1748, TX 78712, USA

are enlisted for the resolution of the wave motion, the only computationally meaningful strategy mandates truncation of the infinite or semi-infinite extent of the originally unbounded domain. Truncation, in turn, introduces artificial boundaries that demand special treatment: the boundaries have to be either transparent to or absorbent of outgoing waves, so that the finite domain of interest ends up mimicking the physics of the originally infinite or semi-infinite domain.

Transparent conditions are, typically, conditions prescribed on the truncation surface, and allow for the passage of the waves without, ideally, any reflections from the truncation surface. Absorbing boundaries or layers require the construction of a buffer zone within which the waves are forced to decay. The terms "transparent" and "absorbing" have been used interchangeably in the literature, together with silent, non-reflecting, transmitting, etc, even though it seems reasonable to reserve "absorbing" for those truncation surface constructs where the wave motion is truly absorbed: this is the terminology we adopt herein. The literature on transparent conditions is considerable: a fairly comprehensive review of various developments up to about 1998 can be found in Tsynkov (1998). In short, transparent conditions can be roughly classified as local or non-local, with the locality referring to how strongly coupled the motion is in both the temporal and spatial sense on the truncation surface. Local conditions are usually less accurate, but computationally friendlier to implement, whereas non-local conditions, including exact conditions whenever available, are more accurate, but computationally onerous. More importantly though, most developments to date, whether pertaining to local or non-local conditions are not capable of handling material heterogeneity, and they are usually predicated upon the assumption of an exterior homogeneous host.

When material heterogeneity is present, and especially when one is interested in direct time-domain simulations, the only presently available approach is based on the concept of Perfectly-Matched-Layers (PMLs), which is an absorbing layer approach, pioneered by Bérenger (1994) for electromagnetics. The key idea is based on enforcement of rapid wave attenuation within buffer zones surrounding the truncation surfaces, while allowing for reflection-less interfaces between the buffer zones and the computational domain of interest. The last fifteen years have seen a wide range of applications of PMLs, including, for example, the linearized Euler equations (Hu, 1996), the simulation of high-power microwaves (HPM) (Wang, Wang, and Zhang, 2006), Helmholtz equation (Turkel and Yefet, 1998; Harari and Albocher, 2006), seismic wave propagation in poroelastic media (Zeng, He, and Liu, 2001), fluid-filled pressurized boreholes (Liu and Sinha, 2003), nonlinear and matter waves (Farrell and Leonhardt, 2005), acoustics (Zampolli, Tesei, and Jensen, 2007), etc. In this work, our focus is on elastodynamics, and in particular on the 3D axisymmetric case (which reduces to a two-dimensional problem); however, to

place our own development in context, we review chronologically related developments in both elastodynamics and electromagnetics, the latter to the extent they have inspired developments in elastodynamics.

Bérenger's (1994) original formulation was based on field-splitting, whereby the contribution of the spatial derivatives of the primary field in each coordinate direction was isolated, yielding two non-physical components for each field. Chew and Weedon (1994) reinterpreted the PML using a complex coordinate-stretching viewpoint, i.e., a mapping of the spatial coordinates onto the complex space via complex stretching functions. Chew and Liu (1996) were the first to extend the PML to elastodynamics. At the same time, in Hastings, Schneider, and Broschat (1996), a PML for elastic waves was developed using displacement potentials in a velocity-stress finite-difference implementation. Later, Gedney (1996) proposed the re-interpretation of the PML as an artificial anisotropic material. The *anisotropic* PML avoided field-splitting and, therefore, it was computationally more efficient when compared to split-field PML developments. Kuzuoglu and Mittra (1996) proposed another form of stretching functions, aiming at rendering the PML causal for transient applications. Though their causality concern was later traced, by Teixeira and Chew (1999), to an error in the application of Kramers-Krönig relationships, the proposed fix resulted in an innovative formulation, later referred to as *complex-frequency-shifted* PML (CFS-PML). However, the time-domain implementation of the CFS-PML proved to be onerous, since it entailed the resolution of convolutions. Roden and Gedney (2000b) suggested a recursive scheme for reducing the computational cost associated with the convolutional operations, and an efficient implementation of the CFS-PML emerged in electromagnetics, henceforth referred to as *convolution* PML (CPML).

The generalization of PML formulations to coordinate systems other than cartesian is of importance for certain problems where the domain of interest is more naturally associated with a non-cartesian coordinate system. In electromagnetics, the cartesian PML, based on the complex coordinate-stretching approach, was extended to cylindrical and spherical coordinates in (Teixeira and Chew, 1997a; Chew, Jin, and Michielssen, 1997; Teixeira and Chew, 1997b,c). As pointed out by Liu and He (1998), the straightforward extension of the original PML formulation to cylindrical coordinates was not reflection-less (thence the name *quasi*-PML in electromagnetics), but it was computationally less demanding when compared against other implementations of the PML in cylindrical coordinates. Next, Liu (1999) developed for the first time a PML for elastodynamics in cylindrical and spherical coordinates based on split fields. The state-of-the-art in the development of PMLs (up to about 2000) was presented by Teixeira and Chew (2000), including a generalization of the PML to cartesian, cylindrical, and spherical coordinates. Independently, Zhao

(2000) derived a PML for general curvilinear coordinates in a systematic manner.

Collino and Tsogka (2001) addressed heterogeneity and anisotropy showing numerically that the PML can efficiently handle both. In a formulation similar to the one presented earlier by Chew and Liu (1996), Collino and Tsogka (2001) discussed a velocity-stress split-field formulation implemented in a finite-difference (FD) time-domain setting. In Bécache, Joly, and Tsogka (2001), a mixed finite-element implementation of the velocity-stress formulation was presented in the context of a fictitious domain method. Komatitsch and Tromp (2003) introduced a new displacement-only split-field formulation, by splitting the displacement field into four components, with the resulting system being either third-order in time, or second-order coupled with one first-order equation. In Bécache, Fauqueux, and Joly (2003), the authors discussed the PML's stability, and the effect of anisotropy: whereas the PML was proved to be stable for any isotropic material, it is, in general, unstable for anisotropic applications (necessary conditions for stability in the form of material constant inequalities were provided).

Since split-field formulations result in substantial computational cost, there is clear need for unsplit-field developments. Wang and Tang (2003) presented the first unsplit finite-difference PML formulation for elastodynamics, extending the recursive integration method of the CPML from electromagnetics. However, the authors used the standard stretching functions rather than the CFS stretching functions associated with the CPML. Recently, Drossaert and Giannopoulos (2007a) implemented the CPML using the CFS stretching functions.

Festa and Nielsen (2003) demonstrated the efficacy of PML even for Rayleigh and interface waves, where both were attenuated remarkably well. The findings of Komatitsch and Tromp (2003) further supported the efficiency of PML in absorbing surface waves, however the authors showed degrading PML performance at grazing incidence. The poor performance of the regularly-stretched PML when waves are incident at near-grazing angles was observed also by Drossaert and Giannopoulos (2007b,a), however, these peculiarities were not detected when CFS stretching functions were used in the CPML implementation. Komatitsch and Martin (2007) and Martin, Komatitsch, and Gedney (2008) also confirmed the superior performance of the CPML implementation even at grazing incidence (the use of CFS stretching functions had already proved its effectiveness in electromagnetics (Roden and Gedney, 2000a; Bérenger, 2002b,a)). In a recent work, Meza-Fajardo and Papageorgiou (2008) proposed the adoption of stretching functions in all directions, i.e., not only along the direction normal to the PML interface, and have showed superior performance of their multi-axial PML (M-PML) when compared against the regularly stretched PML and the CPML.

Basu and Chopra (2003, 2004) developed a displacement-based unsplit-field PML

for time-harmonic and transient elastodynamics using finite elements for the implementation. Though the authors formulated the unsplit-field PML following, initially, a mixed displacement-stress approach, at the discrete level they gravitated towards displacement-based finite-elements, and proposed a complicated time-integration scheme to integrate the resulting semi-discrete forms. Basu (2009) has attempted to improve the performance of the scheme, however the gain is still limited due to the complexity of the displacement-based unsplit-field PML formulation in the time-domain. Cohen and Fauqueux (2005) reported a unique mixed finite-element formulation based on an original decomposition of the elasticity system as a first-order system, where the authors opted for decomposing the strain tensor into components (as opposed to splitting the velocity/stress fields). Festa and Vilotte (2005) discussed a split-field velocity-stress PML formulation, originating from a first-order (in time) decomposition.

In summary, the key PML developments for time-domain elastodynamics can be roughly grouped in four categories: split-field finite difference (Chew and Liu, 1996; Hastings, Schneider, and Broschat, 1996; Liu, 1999; Collino and Tsogka, 2001), split-field finite element (Bécache, Joly, and Tsogka, 2001; Komatitsch and Tromp, 2003; Cohen and Fauqueux, 2005; Festa and Vilotte, 2005; Meza-Fajardo and Papageorgiou, 2008), unsplit-field finite difference (Wang and Tang, 2003; Drossaert and Giannopoulos, 2007b,a; Komatitsch and Martin, 2007), and unsplit-field finite element (Basu and Chopra, 2003, 2004; Basu, 2009). Thus far, too little attention has been paid to unsplit-field PML formulations in transient elastodynamics, and to the best of our knowledge, none has been developed for the axisymmetric case. This paper seeks to fill this gap by providing an unsplit-field axisymmetric PML for transient elastodynamics in a new mixed finite element setting. The motivation derives from both geotechnical and geophysical applications: for example, non-destructive testing and evaluation of pavements is nowadays commonly performed using either stationary or moving loads that give rise to axisymmetric problems. Similarly, in geophysical probing applications, the modeling of wave patterns around boreholes is typically an axisymmetric problem. We favor finite elements for the ease by which they handle arbitrary geometries; we prefer unsplit-fields for the ease by which new developments can be incorporated into existing codes, and for the computational savings they afford when compared to split fields; finally, we favor a mixed method, whereby both displacements and stresses are retained as unknowns, since a single-field approach would greatly complicate time integration (through convolutions or other complexities).

Specifically, we are concerned with elastic wave simulations in semi-infinite, heterogeneous but axisymmetric media, which typically arise in seismic and geophysical applications, geotechnical site characterization, and pavement design or as-

sessment problems. We discuss the development of a new, non-classical, mixed displacement-stress formulation in PML-truncated axisymmetric media for transient elastic wave simulations that results in a semi-discrete form that contains a jerk or jolt term for the displacements. In section 2, we review the basic idea of complex coordinate-stretching to place our own development in context; in section 3, we apply coordinate-stretching to the governing equations in the frequency-domain, and invert back in the time-domain to obtain the axisymmetric unsplit-field PML formulation. The details of the mixed finite element implementation are discussed in section 4. In section 5, we report numerical simulations demonstrating the stability and efficacy of the approach, and in section 6 we conclude with our observations.

2   Complex Coordinate-Stretching

The interpretation of the PML in the context of complex coordinate-stretching by Chew and Weedon (1994) allowed for the PML's wide adoption and refined development. The idea of complex coordinate-stretching is based on analytic continuation of the solutions of wave equations (Teixeira and Chew, 2000), and is realized via a mapping of the spatial coordinates onto the complex space via complex stretching functions. This is accomplished by a simple change of coordinate variables from real to their complex stretched counterparts. The method is applied in the frequency domain, and the resulting system of equations is inverted back into the time-domain for transient applications.

2.1   *Basic idea*

Consider a PML of thickness L_{PML} attached to the computational domain of interest, as depicted in Figure 1. Let s denote the coordinate variable defined along the direction normal to the interface; the interface is located at s_o. The regular domain extends between $0 \leq s < s_o$, and the PML buffer zone occupies $s_o < s \leq s_t$. The key idea is to replace the original coordinate s by a stretched coordinate $\tilde{s}$, wherever s appears in the wave motion governing equations; $\tilde{s}$ is defined as

$$\tilde{s} = \int_0^s \varepsilon_s(s', \omega) \, ds' = s_o + \int_{s_o}^s \varepsilon_s(s', \omega) \, ds', \tag{1}$$

where ω denotes circular frequency, and ε_s denotes a complex stretching function in the direction of s. Though various forms of stretching functions have been proposed, here we adopt the most-widely used form of a stretching function due to its straightforward implementation and improved performance with low-frequency
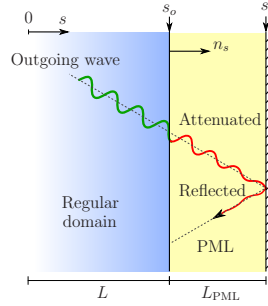
Figure 1: A PML-truncated computational domain in the direction of coordinate s. The outgoing waves pass through the interface located at s_o without reflections, and decay exponentially with distance within the layer.

propagating waves. Accordingly

$$\varepsilon_s(s,\omega) = \alpha_s(s) + \frac{\beta_s(s)}{i\omega},$$ (2)

where α_s and β_s are commonly referred to as scaling (or stretching) and attenuation functions, respectively (both are real-valued). The real part of ε_s scales the coordinate s, and, thus, acts as a real-valued stretch, effectively resulting in artificial geometric damping. However, the amount of attenuation imposed by the scaling function is not enough to attenuate the propagating waves. It is the imaginary part of ε_s that is responsible for the exponential decay of the propagating wave, once it enters the PML. In order not to alter the wave motion (or the governing equations) within the regular domain, $\alpha_s(s) = 1$ and $\beta_s(s) = 0$ for $0 \leq s < s_o$. However, inside the PML, $\alpha_s(s) > 1$ and $\beta_s(s) > 0$, in order to attenuate both the evanescent and propagating waves. At the interface, the continuity is satisfied by $\alpha_s(s_o) = 1$ and $\beta_s(s_o) = 0$. The rate of decay within the PML is frequency-independent, since both the scaling and attenuation functions do not depend on frequency. Although α_s is usually taken as unity, values greater than unity within the PML could improve the attenuation of strong evanescent waves (Liu, 1999).

To introduce the stretched coordinate $\tilde{s}$ in the governing equations, we make use of the fundamental theorem of calculus that suggests

$$\frac{d\tilde{s}}{ds} = \frac{d}{ds} \int_0^s \varepsilon_s(s',\omega)\,ds' = \varepsilon_s(s,\omega) \qquad \Rightarrow \frac{d}{d\tilde{s}} = \frac{1}{\varepsilon_s(s,\omega)} \frac{d}{ds}.$$ (3)

For notational simplicity, we, henceforth, drop the functional dependence of ε_s.

2.2 Choice of stretching function

There is no rigorous methodology suggested in the literature for choosing the scaling and attenuation functions α_s and β_s, respectively, but the key idea is to have a profile varying smoothly with distance within the PML. To minimize reflections, generally, either quadratic or linear profiles have been recommended (Chew and Liu (1996)), though, we have found linear profiles to result in sharp profiles, sharper than higher-order polynomials, thus exacting the mesh requirements within the PML. On the other hand, quadratic profiles have been broadly used in elastodynamics (Collino and Tsogka, 2001; Komatitsch and Tromp, 2003; Cohen and Fauqueux, 2005; Festa and Vilotte, 2005). In general, the commonly adopted form of the attenuation profile can be cast, for arbitrary polynomial degree m, as

$$\beta_s(s) = \begin{cases} 0, & 0 \leq s \leq s_o, \\ \beta_o \left[\frac{(s-s_o)n_s}{L_{\mathrm{PML}}} \right]^m, & s_o < s < s_t, \end{cases} \tag{4}$$

where β_o is a user-chosen scalar parameter, m is the degree of the polynomial attenuation, and n_s is the $s-$th component of the outward normal to the interface between the PML and the regular domain. For ε_s to remain dimensionless, parameter β_o must have units of frequency. Based on one-dimensional wave propagation ideas, β_o can be shown to assume the form

$$\beta_o = \frac{(m+1)c_p}{2L_{\mathrm{PML}}} \log\left(\frac{1}{|R|}\right), \tag{5}$$

where R is user-tunable reflection coefficient controlling the amount of reflections from the outer PML boundary that is typically set as fixed, and c_p is the P-wave velocity (in general, a reference velocity). Once a polynomial degree is specified for the attenuation profile, the strength of decay in the PML can be tuned by controlling R. The scaling function (α_s) controls the decay of evanescent waves and affects the performance of the PML. It is common practice to use similar profiles for both scaling and attenuation functions. Since α_s is required to be unity in the regular domain, a form similar to the attenuation profile β_s requires that α_s be expressed as

$$\alpha_s(s) = \begin{cases} 1, & 0 \leq s \leq s_o, \\ 1 + \alpha_o \left[\frac{(s-s_o)n_s}{L_{\mathrm{PML}}} \right]^m, & s_o < s < s_t, \end{cases} \tag{6}$$

where α_o is, similar to β_o, a user-chosen dimensionless scalar parameter. To avoid having two different tuning parameters, here, we employ a form similar to β_o

$$\alpha_o = \frac{(m+1)b}{2L_{\mathrm{PML}}} \log\left(\frac{1}{|R|}\right), \tag{7}$$

where b is a characteristic length of the domain (e.g., element size). Upon substitution of α_s and β_s in (2), the stretched coordinate $\tilde{s}$ in (1) becomes:

$$\tilde{s} = \int_0^s \left(\alpha_s(s') + \frac{\beta_s(s')}{i\omega} \right) ds' \quad \Rightarrow \quad \tilde{s} = \bar{\alpha}_s + \frac{\bar{\beta}_s}{i\omega}, \tag{8}$$

where $\bar{\alpha}_s(s)$ and $\bar{\beta}_s(s)$ denote the integrated quantities. In this work, we favor quadratic profiles ($m = 2$), even though higher-order profiles enforce more gradual attenuation within the PML. In summary,

$$\alpha_s(s) = \begin{cases} 1, & 0 \le s \le s_o, \\ 1 + \frac{3b}{2L_{\text{PML}}} \log\left(\frac{1}{|R|}\right) \left[\frac{(s-s_o)n_s}{L_{\text{PML}}}\right]^2, & s_o < s < s_t, \end{cases} \tag{9}$$

$$\beta_s(s) = \begin{cases} 0, & 0 \le s \le s_o, \\ \frac{3c_p}{2L_{\text{PML}}} \log\left(\frac{1}{|R|}\right) \left[\frac{(s-s_o)n_s}{L_{\text{PML}}}\right]^2, & s_o < s < s_t. \end{cases} \tag{10}$$

Guided by the numerical experiments that appear later in this article, our experience with a variable α_s parameter shows no significant improvement over a constant α_s of value 1 and we have thus used $\alpha_s(s) = 1$, $0 \le s < s_t$. However, we note that in the presence of strong evanescent waves there may be an advantage in using a spatially varying α_s.

3 Axisymmetric unsplit-field PML

In coordinate-independent form, the propagation of linear elastic waves is governed by the equations of motion, the generalized Hooke's law, and the kinematic conditions

$$\mathbf{div}\,\mathscr{S}^T + \mathbf{f} = \rho\ddot{\mathbf{u}}, \tag{11}$$

$$\mathscr{S} = \mathscr{C} : \mathscr{E}, \tag{12}$$

$$\mathscr{E} = \frac{1}{2}\left[\nabla\mathbf{u} + (\nabla\mathbf{u})^T\right], \tag{13}$$

where $\mathscr{S}$, $\mathscr{E}$, and $\mathscr{C}$ are the stress, strain, and elasticity tensors, respectively. ρ is the density of the elastic medium, $\mathbf{u}$ is the displacement vector, $\mathbf{f}$ is the load vector, (:) denotes tensor inner product, and a dot (˙) denotes differentiation with respect to time of the subtended function. For the axisymmetric problem of interest herein, the above equations must be recast in cylindrical coordinates (r, θ, z), where r denotes radial distance, θ is the polar angle, and z is vertical distance (along the domain's depth); to this end, the gradient of a vector $\mathbf{v}$, and the divergence of a tensor $\mathscr{A}$ are defined as

$$\nabla\mathbf{v} = \frac{1}{h_i}\frac{\partial\mathbf{v}}{\partial i} \otimes \mathbf{e}_i, \qquad \mathbf{div}\,\mathscr{A} = \frac{1}{r}\frac{\partial}{\partial i}\left(r\frac{\mathscr{A}_{ji}}{h_i}\mathbf{e}_j\right), \tag{14}$$

where i and j denote one of r, θ, z, $\mathbf{e}_i$ is the unit vector along the i-axis, repeated indices imply summation, $\otimes$ denotes tensor product, and the scale factors in the case of cylindrical coordinates reduce to $h_r = h_z = 1$, and $h_\theta = r$.

The PML formulation results from the application of complex coordinate-stretching to the governing equations so that the resulting system governs the motion within both the regular and PML domains. To this end, equations (11-13) must be first Fourier-transformed, then stretched, and finally inverted back into the time-domain for transient implementations. Within the regular domain, the stretched equations reduce, by construction of the stretching function ε_s, to the original, undisturbed, system of governing equations.

3.1 Frequency-domain equations

Application of the Fourier transform to the equilibrium, constitutive, and kinematic equations (11-13) results in

$$\mathbf{div}\,\hat{\mathscr{S}}^T + \hat{\mathbf{f}} = -\omega^2 \rho \hat{\mathbf{u}}, \tag{15}$$

$$\hat{\mathscr{S}} = \mathscr{C} : \hat{\mathscr{E}}, \tag{16}$$

$$\hat{\mathscr{E}} = \frac{1}{2}\left[\nabla\hat{\mathbf{u}} + (\nabla\hat{\mathbf{u}})^T\right], \tag{17}$$

where we have assumed initially silent conditions for the displacement field, and a caret (ˆ) denotes the Fourier transform of the subtended function. Next, we apply complex coordinate-stretching by making use of (1), (2), (8), and the definitions (14). Since the problem of interest here is axisymmetric, we apply the stretching only in the r and z coordinates, i.e., in directions normal to the interface between the regular domain and PML, by replacing r and z with the stretched coordinates $\tilde{r}$ and $\tilde{z}$. In unabridged notation the equilibrium equations become

$$\frac{\partial \hat{\sigma}_{rr}}{\partial \tilde{r}} + \frac{\partial \hat{\sigma}_{zr}}{\partial \tilde{z}} + \frac{\hat{\sigma}_{rr}}{\tilde{r}} - \frac{\hat{\sigma}_{\theta\theta}}{\tilde{r}} + \hat{f}_r = -\omega^2 \rho \hat{u}_r, \tag{18}$$

$$\frac{\partial \hat{\sigma}_{rz}}{\partial \tilde{r}} + \frac{\partial \hat{\sigma}_{zz}}{\partial \tilde{z}} + \frac{\hat{\sigma}_{rz}}{\tilde{r}} + \hat{f}_z = -\omega^2 \rho \hat{u}_z, \tag{19}$$

where σ_{ij} denotes the stress tensor component on the plane normal to i in the direction of j $(\sigma_{ij} = (\mathscr{S})_{ij})$. Using (3), the above equations can be expressed in terms of the unstretched coordinates as

$$\frac{1}{\varepsilon_r}\frac{\partial \hat{\sigma}_{rr}}{\partial r} + \frac{1}{\varepsilon_z}\frac{\partial \hat{\sigma}_{zr}}{\partial z} + \frac{\hat{\sigma}_{rr}}{\tilde{r}} - \frac{\hat{\sigma}_{\theta\theta}}{\tilde{r}} + \hat{f}_r = -\omega^2 \rho \hat{u}_r, \tag{20}$$

$$\frac{1}{\varepsilon_r}\frac{\partial \hat{\sigma}_{rz}}{\partial r} + \frac{1}{\varepsilon_z}\frac{\partial \hat{\sigma}_{zz}}{\partial z} + \frac{\hat{\sigma}_{rz}}{\tilde{r}} + \hat{f}_z = -\omega^2 \rho \hat{u}_z. \tag{21}$$

Next, we multiply both sides by $\varepsilon_r \varepsilon_z \frac{\tilde{r}}{r}$. Using again the definition of divergence (14), the equations of equilibrium can be compactly recast as

$$\mathbf{div}\left(\hat{\mathscr{S}}^T \tilde{\Lambda}\right) + \varepsilon_r \varepsilon_z \frac{\tilde{r}}{r}\hat{\mathbf{f}} = -\omega^2 \rho \varepsilon_r \varepsilon_z \frac{\tilde{r}}{r}\hat{\mathbf{u}}, \tag{22}$$

where, after making use of (2) and (8), $\tilde{\Lambda}$ is defined as

$$\tilde{\Lambda} = \begin{bmatrix} \varepsilon_z \frac{\tilde{r}}{r} & 0 & 0 \\ 0 & \varepsilon_r \varepsilon_z & 0 \\ 0 & 0 & \varepsilon_r \frac{\tilde{r}}{r} \end{bmatrix} = \begin{bmatrix} \frac{\alpha_z \bar{\alpha}_r}{r} & 0 & 0 \\ 0 & \alpha_r \alpha_z & 0 \\ 0 & 0 & \frac{\alpha_r \bar{\alpha}_r}{r} \end{bmatrix} + \frac{1}{(i\omega)^2}\begin{bmatrix} \frac{\bar{\beta}_r \beta_z}{r} & 0 & 0 \\ 0 & \beta_r \beta_z & 0 \\ 0 & 0 & \frac{\beta_r \bar{\beta}_r}{r} \end{bmatrix} +$$

$$\frac{1}{i\omega}\begin{bmatrix} \frac{\alpha_z \bar{\beta}_r + \beta_z \bar{\alpha}_r}{r} & 0 & 0 \\ 0 & \alpha_r \beta_z + \beta_r \alpha_z & 0 \\ 0 & 0 & \frac{\alpha_r \bar{\beta}_r + \beta_r \bar{\alpha}_r}{r} \end{bmatrix} = \tilde{\Lambda}_e + \frac{1}{i\omega}\tilde{\Lambda}_p + \frac{1}{(i\omega)^2}\tilde{\Lambda}_w. \tag{23}$$

In the above, subscripts "e" and "p" refer to attenuation functions associated with evanescent and propagating waves, respectively. We remark that in the regular domain, $\tilde{\Lambda}_e$ reduces to the identity tensor, whereas $\tilde{\Lambda}_p$ and $\tilde{\Lambda}_w$ vanish identically. After substituting (23) into (22), using (2) and (8), multiplying both sides by $i\omega$, rearranging and grouping like-terms, there results

$$\mathbf{div}\left(i\omega \hat{\mathscr{S}}^T \tilde{\Lambda}_e + \hat{\mathscr{S}}^T \tilde{\Lambda}_p + \frac{1}{i\omega}\hat{\mathscr{S}}^T \tilde{\Lambda}_w\right) + i\omega a\hat{\mathbf{f}} + b\hat{\mathbf{f}} + \frac{c}{i\omega}\hat{\mathbf{f}} + \frac{d}{(i\omega)^2}\hat{\mathbf{f}} =$$
$$\rho\left[(i\omega)^3 a\hat{\mathbf{u}} + (i\omega)^2 b\hat{\mathbf{u}} + i\omega c\hat{\mathbf{u}} + d\hat{\mathbf{u}}\right], \tag{24}$$

where

$$a = \frac{\alpha_r \alpha_z \bar{\alpha}_r}{r}, \quad b = \frac{\alpha_r \alpha_z \bar{\beta}_r + \bar{\alpha}_r \alpha_r \beta_z + \alpha_z \bar{\alpha}_r \beta_r}{r},$$
$$c = \frac{\alpha_r \bar{\beta}_r \beta_z + \bar{\alpha}_r \beta_z \beta_r + \alpha_z \beta_r \bar{\beta}_r}{r}, \quad d = \frac{\beta_r \bar{\beta}_r \beta_z}{r}. \tag{25}$$

We note that, within the regular domain, $a \equiv 1, b \equiv 0, c \equiv 0, d \equiv 0$, and since the body forces $\mathbf{f}$ are non-vanishing only within the regular domain ($\mathbf{f}$ vanishes within the PML), (24) reduces further to:

$$\mathbf{div}\left(i\omega \hat{\mathscr{S}}^T \tilde{\Lambda}_e + \hat{\mathscr{S}}^T \tilde{\Lambda}_p + \frac{1}{i\omega}\hat{\mathscr{S}}^T \tilde{\Lambda}_w\right) + i\omega a\hat{\mathbf{f}} =$$
$$\rho\left[(i\omega)^3 a\hat{\mathbf{u}} + (i\omega)^2 b\hat{\mathbf{u}} + i\omega c\hat{\mathbf{u}} + d\hat{\mathbf{u}}\right], \tag{26}$$

Similarly, we apply complex coordinate-stretching to the kinematic equation (13), while also implicitly defining a new stretching tensor Λ; there results

$$\hat{\mathscr{E}} = \frac{1}{2} \left\{ (\nabla \hat{\mathbf{u}}) \begin{bmatrix} \frac{1}{\varepsilon_r} & 0 & 0 \\ 0 & \frac{r}{\tilde{r}} & 0 \\ 0 & 0 & \frac{1}{\varepsilon_z} \end{bmatrix} + \begin{bmatrix} \frac{1}{\varepsilon_r} & 0 & 0 \\ 0 & \frac{r}{\tilde{r}} & 0 \\ 0 & 0 & \frac{1}{\varepsilon_z} \end{bmatrix} (\nabla \hat{\mathbf{u}})^T \right\} = \frac{1}{2} \left[(\nabla \hat{\mathbf{u}}) \Lambda + \Lambda^T (\nabla \hat{\mathbf{u}})^T \right].$$

(27)

Next, we pre- and post-multiply (27) by $i\omega\Lambda^{-T}$ and Λ^{-1}, respectively, to obtain

$$i\omega\Lambda^{-T} \hat{\mathscr{E}} \Lambda^{-1} = \frac{1}{2} i\omega \left[\Lambda^{-T} (\nabla \hat{\mathbf{u}}) + (\nabla \hat{\mathbf{u}})^T \Lambda^{-1} \right],$$

(28)

where

$$\Lambda^{-1} = \begin{bmatrix} \varepsilon_r & 0 & 0 \\ 0 & \frac{\tilde{r}}{r} & 0 \\ 0 & 0 & \varepsilon_z \end{bmatrix} = \begin{bmatrix} \alpha_r & 0 & 0 \\ 0 & \frac{\bar{\alpha}_r}{r} & 0 \\ 0 & 0 & \alpha_z \end{bmatrix} + \frac{1}{i\omega} \begin{bmatrix} \beta_r & 0 & 0 \\ 0 & \frac{\bar{\beta}_r}{r} & 0 \\ 0 & 0 & \beta_z \end{bmatrix} = \Lambda_e + \frac{1}{i\omega} \Lambda_p.$$

(29)

Substituting (29) into (28), rearranging and grouping like-terms, yields

$$i\omega\Lambda_e^T \hat{\mathscr{E}} \Lambda_e + \Lambda_e^T \hat{\mathscr{E}} \Lambda_p + \Lambda_p^T \hat{\mathscr{E}} \Lambda_e + \frac{1}{i\omega} \Lambda_p^T \hat{\mathscr{E}} \Lambda_p =$$

$$\frac{1}{2} \left[\Lambda_p^T (\nabla \hat{\mathbf{u}}) + (\nabla \hat{\mathbf{u}})^T \Lambda_p \right] + \frac{1}{2} i\omega \left[\Lambda_e^T (\nabla \hat{\mathbf{u}}) + (\nabla \hat{\mathbf{u}})^T \Lambda_e \right].$$

(30)

Equations (26), (16), and (30), constitute the stretched form of the governing frequency-domain equations.

3.2   Time-domain equations

By taking the inverse Fourier transform of (26), (16), and (30), there results

$$\mathbf{div} \left[\dot{\mathscr{S}}^T \tilde{\Lambda}_e + \mathscr{S}^T \tilde{\Lambda}_p + \left(\int_0^t \mathscr{S}^T d\tau \right) \tilde{\Lambda}_w \right] + a\dot{\mathbf{f}} = \rho \left[a\,\dddot{\mathbf{u}} + b\ddot{\mathbf{u}} + c\dot{\mathbf{u}} + d\mathbf{u} \right],$$

(31)

$$\mathscr{S} = \mathscr{C} : \mathscr{E},$$

(32)

$$\Lambda_e^T \dot{\mathscr{E}} \Lambda_e + \Lambda_e^T \mathscr{E} \Lambda_p + \Lambda_p^T \mathscr{E} \Lambda_e + \Lambda_p^T \left(\int_0^t \mathscr{E} d\tau \right) \Lambda_p =$$

$$\frac{1}{2} \left[\Lambda_p^T (\nabla \mathbf{u}) + (\nabla \mathbf{u})^T \Lambda_p \right] + \frac{1}{2} \left[\Lambda_e^T (\nabla \dot{\mathbf{u}}) + (\nabla \dot{\mathbf{u}})^T \Lambda_e \right],$$

(33)

where we used the following inverse Fourier transform property valid for any function $g(t)$ satisfying the usual requirements:

$$\mathscr{F}^{-1} \left[\frac{\hat{g}(\omega)}{i\omega} \right] = \int_0^t g(\tau) d\tau,$$

(34)

where $\mathscr{F}^{-1}$ denotes the inverse Fourier operator[1].

Notice that the equilibrium equation (31) implicates a jerk term for the displacements; to retain second-order derivatives as the highest derivatives in the formulation, we express the displacements in terms of the velocities, by introducing $\bar{\mathbf{v}}$ as:

$$\mathbf{u}(\mathbf{x},t) = \bar{\mathbf{v}}(\mathbf{x},t) = \int_0^t \mathbf{v}(\mathbf{x},\tau)d\tau. \tag{35}$$

Next, we define the following stress and strain memory (or history) tensor terms:

$$\mathbf{S}(\mathbf{x},t) = \int_0^t \mathscr{S}(\mathbf{x},\tau)d\tau, \quad \mathbf{E}(\mathbf{x},t) = \int_0^t \mathscr{E}(\mathbf{x},\tau)d\tau, \tag{36}$$

which are such that

$$\dot{\mathbf{S}}(\mathbf{x},t) = \mathscr{S}(\mathbf{x},t), \quad \ddot{\mathbf{S}}(\mathbf{x},t) = \dot{\mathscr{S}}(\mathbf{x},t), \quad \dot{\mathbf{E}}(\mathbf{x},t) = \mathscr{E}(\mathbf{x},t), \quad \ddot{\mathbf{E}}(\mathbf{x},t) = \dot{\mathscr{E}}(\mathbf{x},t). \tag{37}$$

Substitution of (35), (36) and (37) into (31-33) leads to the time-domain equations of our axisymmetric unsplit-field PML formulation

$$\mathbf{div}\left(\ddot{\mathbf{S}}^T\tilde{\Lambda}_e + \dot{\mathbf{S}}^T\tilde{\Lambda}_p + \mathbf{S}^T\tilde{\Lambda}_w\right) + a\dot{\mathbf{f}} = \rho\left(a\ddot{\mathbf{v}} + b\dot{\mathbf{v}} + c\mathbf{v} + d\bar{\mathbf{v}}\right), \tag{38}$$

$$\dot{\mathbf{S}} = \mathscr{C}:\dot{\mathbf{E}}, \tag{39}$$

$$\Lambda_e^T\ddot{\mathbf{E}}\Lambda_e + \Lambda_e^T\dot{\mathbf{E}}\Lambda_p + \Lambda_p^T\dot{\mathbf{E}}\Lambda_e + \Lambda_p^T\mathbf{E}\Lambda_p =$$
$$\frac{1}{2}\left[\Lambda_p^T(\nabla\bar{\mathbf{v}}) + (\nabla\bar{\mathbf{v}})^T\Lambda_p\right] + \frac{1}{2}\left[\Lambda_e^T(\nabla\mathbf{v}) + (\nabla\mathbf{v})^T\Lambda_e\right]. \tag{40}$$

4 Mixed finite element implementation

Owing to the complexity of (38-40), one could not conceivably reduce the set (38-40) to a single unknown field, as it is routinely done in interior displacement-based elastodynamics problems where there is no PML involved. Here, we propose a mixed method approach, whereby we retain both displacements and stresses (or, more appropriately, velocities and stress histories) as unknowns. To this end, we introduce the constitutive law (39) into the kinematic condition (40), to arrive at

$$\mathbf{div}\left(\ddot{\mathbf{S}}^T\tilde{\Lambda}_e + \dot{\mathbf{S}}^T\tilde{\Lambda}_p + \mathbf{S}^T\tilde{\Lambda}_w\right) + a\dot{\mathbf{f}} = \rho\left(a\ddot{\mathbf{v}} + b\dot{\mathbf{v}} + c\mathbf{v} + d\bar{\mathbf{v}}\right), \tag{41}$$

$$\Lambda_e^T(\mathscr{D}:\ddot{\mathbf{S}})\Lambda_e + \Lambda_e^T(\mathscr{D}:\dot{\mathbf{S}})\Lambda_p + \Lambda_p^T(\mathscr{D}:\dot{\mathbf{S}})\Lambda_e + \Lambda_p^T(\mathscr{D}:\mathbf{S})\Lambda_p =$$
$$\frac{1}{2}\left[\Lambda_p^T(\nabla\bar{\mathbf{v}}) + (\nabla\bar{\mathbf{v}})^T\Lambda_p\right] + \frac{1}{2}\left[\Lambda_e^T(\nabla\mathbf{v}) + (\nabla\mathbf{v})^T\Lambda_e\right], \tag{42}$$

---

[1] In general, $\mathscr{F}^{-1}\left[\frac{\hat{g}(\omega)}{i\omega}\right] = \int_0^t g(\tau)d\tau - \pi\hat{g}(0)\delta(\omega)$, but, it can be shown that since, by construction, the overall development excludes $\omega = 0$, the inverse transform reduces to (34).
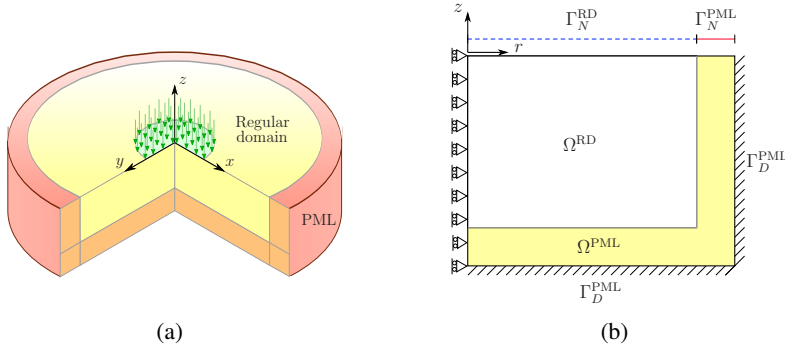
Figure 2: A PML-truncated axisymmetric semi-infinite homogeneous elastic domain. (a) Three-dimensional model, (b) Computational model with the symmetry conditions introduced on the left-boundary.

where $\mathscr{D}$ denotes the compliance tensor ($\mathbf{E} = \mathscr{D} : \mathbf{S}$). Consider next the half-space problem depicted in Figure 2. Let $\Omega^{\text{RD}} \cup \Omega^{\text{PML}} = \Omega \subset \mathfrak{R}^3$ denote the region occupied by the elastic body $(\Omega^{\text{RD}})^2$, surrounded on its periphery and bottom by the PML buffer zone (Ω^{PML}). Ω is bounded by $\Gamma = \Gamma_D \cup \Gamma_N$, where $\Gamma_D \cap \Gamma_N = \emptyset$, and $\Gamma_D \equiv \Gamma_D^{\text{PML}}$, $\Gamma_N = \Gamma_N^{\text{RD}} \cup \Gamma_N^{\text{PML}}$. Moreover, let $\mathsf{J} = (0, T]$ denote the time interval of interest. Then, we require that (41-42) hold in $\Omega \times \mathsf{J}$, subject to the following boundary and initial conditions:

$$\bar{\mathbf{v}}(\mathbf{x}, t) = \mathbf{0} \qquad \text{on } \Gamma_D^{\text{PML}} \times \mathsf{J}, \tag{43}$$

$$\left(\ddot{\mathbf{S}}^T \tilde{\Lambda}_e + \dot{\mathbf{S}}^T \tilde{\Lambda}_p + \mathbf{S}^T \tilde{\Lambda}_w \right) \mathbf{n} = \mathbf{0} \qquad \text{on } \Gamma_N^{\text{PML}} \times \mathsf{J}, \tag{44}$$

$$\dot{\mathbf{S}}(\mathbf{x}, t)^T \mathbf{n} = g_n(\mathbf{x}, t) \qquad \text{on } \Gamma_N^{\text{RD}} \times \mathsf{J}, \tag{45}$$

$$\bar{\mathbf{v}}(\mathbf{x}, 0) = \mathbf{0}, \quad \mathbf{v}(\mathbf{x}, 0) = \mathbf{0}, \quad \dot{\mathbf{v}}(\mathbf{x}, 0) = \mathbf{0}, \quad \mathbf{S}(\mathbf{x}, 0) = \mathbf{0}, \quad \dot{\mathbf{S}}(\mathbf{x}, 0) = \mathbf{0} \quad \text{in } \Omega, \tag{46}$$

where g_n denotes prescribed tractions on Γ_N^{RD}.

We seek next the weak form, in the Galerkin sense, corresponding to the strong form (41-46). Since both displacements (or velocities) and stresses are retained as independent unknowns, the resulting problem is mixed (Atluri, Gallagher, and Zienkiewicz (1983)), as opposed to single-field problems. In a review of mixed problems by Brezzi (1988), the author pointed out that there exist two possible weak forms for treating a mixed problem, such as the one arising in elastodynamics; the two forms result in *decidedly different* regularity requirements for the approximants. In the first form the regularity required for the stress approximants is *higher* than that of the displacement approximants; this is the classic mixed method. This

---

[2] RD stands for Regular Domain.

form requires special finite elements, such as those first introduced by Raviart and Thomas (1977) for second-order elliptic problems (RT elements). Later on, several other special mixed finite elements were introduced: by Johnson and Mercier (1978), by Brezzi, Douglas, and Marini (1985) (Brezzi-Douglas-Marini BDM), by Arnold, Brezzi, and Fortin (1984) (MINI element), by Arnold, Brezzi, and Douglas (1984) (PEERS, plane elasticity element with reduced symmetry), etc.

On the other hand, in the second form, which differs from the first simply by an integration by parts, the regularity requirements are somewhat reversed: the regularity for the displacement approximants should be *higher* than that of the stress approximants. The latter requirements are less onerous for implementation purposes, and do not require any special element types, such as the RT, BDM, etc. In this work, we favor this second, and largely unexplored, variational form. To this end, we take inner products of the equilibrium equation (41), and the kinematic equation (42) with arbitrary weight functions $\mathbf{w}(\mathbf{x})$ and $\mathbf{T}(\mathbf{x})$, respectively, residing in appropriate admissible spaces, and then integrate over the entire computational domain Ω. In the first weak form that leads to the classic mixed method, integration by parts is applied to the (weighted form of the) kinematic equation only. By contrast, in the second weak form, which we adopt herein, integration by parts is applied to the (weighted form of the) equilibrium equation only. There results

$$\int_\Omega \nabla \mathbf{w} : \left(\ddot{\mathbf{S}}^T \tilde{\Lambda}_e + \dot{\mathbf{S}}^T \tilde{\Lambda}_p + \mathbf{S}^T \tilde{\Lambda}_w \right) \mathrm{d}\Omega + \int_\Omega \mathbf{w} \cdot \rho \; (a\ddot{\mathbf{v}} + b\dot{\mathbf{v}} + c\mathbf{v} + d\bar{\mathbf{v}}) \, \mathrm{d}\Omega =$$
$$\int_{\Gamma_N} \mathbf{w} \cdot \left(\ddot{\mathbf{S}}^T \tilde{\Lambda}_e + \dot{\mathbf{S}}^T \tilde{\Lambda}_p + \mathbf{S}^T \tilde{\Lambda}_w \right) \mathbf{n} \, \mathrm{d}\Gamma + \int_\Omega \mathbf{w} \cdot a\dot{\mathbf{f}} \, \mathrm{d}\Omega, \qquad (47)$$

$$\int_\Omega \left(\mathscr{D} : \ddot{\mathbf{S}} \right) : \Lambda_e \mathbf{T} \Lambda_e^T \, \mathrm{d}\Omega + \int_\Omega \left(\mathscr{D} : \dot{\mathbf{S}} \right) : \left(\Lambda_e \mathbf{T} \Lambda_p^T + \Lambda_p \mathbf{T} \Lambda_e^T \right) \, \mathrm{d}\Omega +$$
$$\int_\Omega \left(\mathscr{D} : \mathbf{S} \right) : \Lambda_p \mathbf{T} \Lambda_p^T \, \mathrm{d}\Omega = \int_\Omega \nabla \bar{\mathbf{v}} : \Lambda_p \mathbf{T}_{sym} \, \mathrm{d}\Omega + \int_\Omega \nabla \mathbf{v} : \Lambda_e \mathbf{T}_{sym} \, \mathrm{d}\Omega, \qquad (48)$$

where $\mathbf{T}_{sym}$ is the symmetric part of tensor $\mathbf{T}$. We seek $\mathbf{v} \in \mathbf{H}^1(\Omega) \times \mathsf{J}$ satisfying $\bar{\mathbf{v}}|_{\Gamma_D^{\mathrm{PML}}} = \mathbf{0}$, and $\mathbf{S} \in \mathscr{L}^2(\Omega) \times \mathsf{J}$ such that equation (48) holds for all $\mathbf{w} \in \mathbf{H}^1(\Omega)$ satisfying $\mathbf{w}|_{\Gamma_D} = \mathbf{0}$ and $\mathbf{T} \in \mathscr{L}^2(\Omega)$. The functional spaces of relevance here are defined, as usual, for scalar functions v, for vector functions $\mathbf{v}$, and tensor functions $\mathscr{A}$, by

$$L^2(\Omega) = \left\{ v : \int_\Omega |v|^2 d\mathbf{x} < \infty \right\}, \quad \mathscr{L}^2(\Omega) = \left\{ \mathscr{A} : \mathscr{A} \in (L^2(\Omega))^{3 \times 3} \right\}, \qquad (49)$$

$$H^1(\Omega) = \left\{ v : \int_\Omega \left(|v|^2 + |\nabla v|^2 \right) d\mathbf{x} < \infty \right\}, \quad \mathbf{H}^1(\Omega) = \left\{ \mathbf{v} : \mathbf{v} \in (H^1(\Omega))^2 \right\}. \qquad (50)$$

It is important to notice that the regularity required for the stresses is *lower* than what is required of the displacements/velocities. Next, we seek approximate solu-

tions for $\mathbf{v}(\mathbf{x},t)$ and $\mathbf{S}(\mathbf{x},t)$; to this end, we introduce the finite-dimensional spaces $\Xi^h \subset \mathbf{H}^1(\Omega)$ and $\Upsilon^h \subset \mathscr{L}^2(\Omega)$. Let the basis functions in Ξ^h and Υ^h be denoted by Φ and Ψ, respectively. The trial functions $\mathbf{v}_h \in \Xi^h \times \mathsf{J}$ and $\mathbf{S}_h \in \Upsilon^h \times \mathsf{J}$ are spatially discretized as

$$\mathbf{v}(\mathbf{x},t) \cong \mathbf{v}_h(\mathbf{x},t) = \begin{bmatrix} \Phi^T(\mathbf{x})\mathbf{v}_r(t) \\ \Phi^T(\mathbf{x})\mathbf{v}_z(t) \end{bmatrix},$$

$$\mathbf{S}(\mathbf{x},t) \cong \mathbf{S}_h(\mathbf{x},t) = \begin{bmatrix} \Psi^T(\mathbf{x})\mathbf{S}_{rr}(t) & 0 & \Psi^T(\mathbf{x})\mathbf{S}_{rz}(t) \\ 0 & \Psi^T(\mathbf{x})\mathbf{S}_{\theta\theta}(t) & 0 \\ \Psi^T(\mathbf{x})\mathbf{S}_{zr}(t) & 0 & \Psi^T(\mathbf{x})\mathbf{S}_{zz}(t) \end{bmatrix}. \tag{51}$$

Similarly, the test functions $\mathbf{w} \in \Xi^h$ and $\mathbf{T} \in \Upsilon^h$ are expressed as

$$\mathbf{w}(\mathbf{x}) \cong \mathbf{w}_h(\mathbf{x}) = \begin{bmatrix} \mathbf{w}_r^T\Phi(\mathbf{x}) \\ \mathbf{w}_z^T\Phi(\mathbf{x}) \end{bmatrix}, \quad \mathbf{T}(\mathbf{x}) \cong \mathbf{T}_h(\mathbf{x}) = \begin{bmatrix} \mathbf{T}_{rr}^T\Psi(\mathbf{x}) & 0 & \mathbf{T}_{rz}^T\Psi(\mathbf{x}) \\ 0 & \mathbf{T}_{\theta\theta}^T\Psi(\mathbf{x}) & 0 \\ \mathbf{T}_{zr}^T\Psi(\mathbf{x}) & 0 & \mathbf{T}_{zz}^T\Psi(\mathbf{x}) \end{bmatrix}. \tag{52}$$

By introducing the symmetry of the stress tensor ($\mathscr{S}^T = \mathscr{S}$), we obtain the *semi-discrete form*

$$\{\mathscr{M}\}\ddot{\mathbf{d}} + \{\mathscr{C}\}\dot{\mathbf{d}} + \{\mathscr{K}\}\mathbf{d} + \{\mathscr{G}\}\bar{\mathbf{d}} = \{\mathscr{R}\}, \tag{53}$$

where

$$\bar{\mathbf{d}} = [\bar{\mathbf{v}}_r\ \bar{\mathbf{v}}_z\ \bar{\mathbf{S}}_{rr}\ \bar{\mathbf{S}}_{\theta\theta}\ \bar{\mathbf{S}}_{zz}\ \bar{\mathbf{S}}_{rz}]^T,$$

$$\mathcal{M} = \begin{bmatrix} \mathbf{M}_a & \mathbf{0} & \mathbf{A}_{e1r} & \mathbf{P}_{e2} & \mathbf{0} & \mathbf{A}_{e3z} \\ \mathbf{0} & \mathbf{M}_a & \mathbf{0} & \mathbf{0} & \mathbf{A}_{e3z} & \mathbf{A}_{e1r} \\ \mathbf{0} & \mathbf{0} & \mathbf{N}_{e1e1} & -\mathbf{Z}_{e1e1} & -\mathbf{Z}_{e1e1} & \mathbf{0} \\ \mathbf{0} & \mathbf{0} & -\mathbf{Z}_{e2e2} & \mathbf{N}_{e2e2} & -\mathbf{Z}_{e2e2} & \mathbf{0} \\ \mathbf{0} & \mathbf{0} & -\mathbf{Z}_{e3e3} & -\mathbf{Z}_{e3e3} & \mathbf{N}_{e3e3} & \mathbf{0} \\ \mathbf{0} & \mathbf{0} & \mathbf{0} & \mathbf{0} & \mathbf{0} & \mathbf{G}_{e1e3} \end{bmatrix},$$

$$\mathcal{C} = \begin{bmatrix} \mathbf{M}_b & \mathbf{0} & \mathbf{A}_{p1r} & \mathbf{P}_{p2} & \mathbf{0} & \mathbf{A}_{p3z} \\ \mathbf{0} & \mathbf{M}_b & \mathbf{0} & \mathbf{0} & \mathbf{A}_{p3z} & \mathbf{A}_{p1r} \\ \mathbf{0} & \mathbf{0} & 2\mathbf{N}_{e1p1} & -2\mathbf{Z}_{e1p1} & -2\mathbf{Z}_{e1p1} & \mathbf{0} \\ \mathbf{0} & \mathbf{0} & -2\mathbf{Z}_{e2p2} & 2\mathbf{N}_{e2p2} & -2\mathbf{Z}_{e2p2} & \mathbf{0} \\ \mathbf{0} & \mathbf{0} & -2\mathbf{Z}_{e3p3} & -2\mathbf{Z}_{e3p3} & 2\mathbf{N}_{e3p3} & \mathbf{0} \\ \mathbf{0} & \mathbf{0} & \mathbf{0} & \mathbf{0} & \mathbf{0} & (\mathbf{G}_{e1p3} + \mathbf{G}_{p1e3}) \end{bmatrix},$$

$$\mathcal{K} = \begin{bmatrix} \mathbf{M}_c & \mathbf{0} & \mathbf{A}_{w1r} & \mathbf{P}_{w2} & \mathbf{0} & \mathbf{A}_{w3z} \\ \mathbf{0} & \mathbf{M}_c & \mathbf{0} & \mathbf{0} & \mathbf{A}_{w3z} & \mathbf{A}_{w1r} \\ -\mathbf{B}_{e1r} & \mathbf{0} & \mathbf{N}_{p1p1} & -\mathbf{Z}_{p1p1} & -\mathbf{Z}_{p1p1} & \mathbf{0} \\ -\mathbf{Q}_{e2} & \mathbf{0} & -\mathbf{Z}_{p2p2} & \mathbf{N}_{p2p2} & -\mathbf{Z}_{p2p2} & \mathbf{0} \\ \mathbf{0} & -\mathbf{B}_{e3z} & -\mathbf{Z}_{p3p3} & -\mathbf{Z}_{p3p3} & \mathbf{N}_{p3p3} & \mathbf{0} \\ -\mathbf{B}_{e1z} & -\mathbf{B}_{e3r} & \mathbf{0} & \mathbf{0} & \mathbf{0} & \mathbf{G}_{p1p3} \end{bmatrix},$$

$$\mathcal{G} = \begin{bmatrix} \mathbf{M}_d & \mathbf{0} & \mathbf{0} & \mathbf{0} & \mathbf{0} & \mathbf{0} \\ \mathbf{0} & \mathbf{M}_d & \mathbf{0} & \mathbf{0} & \mathbf{0} & \mathbf{0} \\ -\mathbf{B}_{p1r} & \mathbf{0} & \mathbf{0} & \mathbf{0} & \mathbf{0} & \mathbf{0} \\ -\mathbf{Q}_{p2} & \mathbf{0} & \mathbf{0} & \mathbf{0} & \mathbf{0} & \mathbf{0} \\ \mathbf{0} & -\mathbf{B}_{p3z} & \mathbf{0} & \mathbf{0} & \mathbf{0} & \mathbf{0} \\ -\mathbf{B}_{p1z} & -\mathbf{B}_{p3r} & \mathbf{0} & \mathbf{0} & \mathbf{0} & \mathbf{0} \end{bmatrix},$$

$$\mathcal{R} = [\mathbf{f^e}_r\ \mathbf{f^e}_z\ \mathbf{0}\ \mathbf{0}\ \mathbf{0}\ \mathbf{0}]^T. \tag{54}$$

The various matrix and vector blocks are defined as

$$\mathbf{f^e}_r = \int_{\Gamma_N^{RD}} \Phi\, g_r(\mathbf{x},t)\, d\Gamma + \int_{\Omega} \Phi a \dot{f}_r\, d\Omega,\ \mathbf{f^e}_z = \int_{\Gamma_N^{RD}} \Phi\, g_z(\mathbf{x},t)\, d\Gamma + \int_{\Omega} \Phi a \dot{f}_z\, d\Omega, \tag{55}$$

and

$$\mathbf{A}_{ijk} = \int_{\Omega} \tilde{\Lambda}_i^j \frac{\partial \Phi}{\partial k} \Psi^T \, d\Omega, \; \mathbf{N}_{ijkl} = \int_{\Omega} \frac{\Lambda_i^j \Lambda_k^l}{E} \Psi \Psi^T \, d\Omega, \; \mathbf{Z}_{ijkl} = \int_{\Omega} \nu \frac{\Lambda_i^j \Lambda_k^l}{E} \Psi \Psi^T \, d\Omega, \tag{56}$$

$$\mathbf{B}_{ijk} = \int_{\Omega} \Lambda_i^j \Psi \frac{\partial \Phi^T}{\partial k} \, d\Omega, \; \mathbf{G}_{ijkl} = \int_{\Omega} 2(1+\nu) \frac{\Lambda_i^j \Lambda_k^l}{E} \Psi \Psi^T \, d\Omega, \tag{57}$$

$$\mathbf{P}_{ij} = \int_{\Omega} \frac{1}{r} \tilde{\Lambda}_i^j \Phi \Psi^T \, d\Omega, \; \mathbf{Q}_{ij} = \int_{\Omega} \frac{1}{r} \Lambda_i^j \Psi \Phi^T \, d\Omega, \; \mathbf{M}_i = \int_{\Omega} i \, \rho \Phi \Phi^T \, d\Omega. \tag{58}$$

Notice that Λ^n and $\tilde{\Lambda}^n$ denote the nth component of the diagonal matrices Λ and $\tilde{\Lambda}$, respectively.

The lowest-order time derivatives implicated in the semi-discrete form (53) are associated with $\bar{\mathbf{d}}$, which, in turn, involve displacements, and time-integrals of the stress history terms. Thus, clearly, the form (53) is unconventional and calls for a specialized time-integration scheme. To this end, we develop an extension to the classical Newmark-β scheme, by, first, making use of the following finite difference formulas describing the evolution of the corresponding quantities

$$\bar{\mathbf{d}}_{n+1} = \bar{\mathbf{d}}_n + \Delta t \, \mathbf{d}_n + \frac{\Delta t^2}{2} \dot{\mathbf{d}}_n + \left(\frac{1}{6} - \alpha \right) \Delta t^3 \ddot{\mathbf{d}}_n + \alpha \, \Delta t^3 \ddot{\mathbf{d}}_{n+1}, \tag{59}$$

$$\mathbf{d}_{n+1} = \mathbf{d}_n + \Delta t \, \dot{\mathbf{d}}_n + \left(\frac{1}{2} - \beta \right) \Delta t^2 \ddot{\mathbf{d}}_n + \beta \, \Delta t^2 \ddot{\mathbf{d}}_{n+1}, \tag{60}$$

$$\dot{\mathbf{d}}_{n+1} = \dot{\mathbf{d}}_n + (1-\gamma) \Delta t \, \ddot{\mathbf{d}}_n + \gamma \, \Delta t \, \ddot{\mathbf{d}}_{n+1}, \tag{61}$$

where Δt denotes the time step, and subscripts (n) and $(n+1)$ denote current and next time step, respectively (β, and γ are the usual Newmark-β parameters, and α is a new Newmark-like parameter). For the linear acceleration method, (α, β, γ) reduce to $(\frac{1}{24}, \frac{1}{6}, \frac{1}{2})$, whereas in the case of the constant (average) acceleration method, (α, β, γ) reduce to $(\frac{1}{12}, \frac{1}{4}, \frac{1}{2})$. Next, after rewriting (53) for the $(n+1)$-th time step, and, subsequently, introducing (59-61), there result the following effective system matrix $\{\mathbf{K}^{\mathbf{eff}}\}$, and effective load vector $\{\mathbf{R}^{\mathbf{eff}}\}_{n+1}$

$$\{\mathbf{K}^{\mathbf{eff}}\} \, \ddot{\mathbf{d}}_{n+1} = \{\mathbf{R}^{\mathbf{eff}}\}_{n+1}, \tag{62}$$

where

$$\{\mathbf{K}^{\mathbf{eff}}\} = \{\mathscr{M}\} + \{\mathscr{C}\}\,\gamma\Delta t + \{\mathscr{K}\}\,\beta\Delta t^2 + \{\mathscr{G}\}\,\alpha\Delta t^3, \tag{63}$$

$$\begin{aligned}
\{\mathbf{R}^{\mathbf{eff}}\}_{n+1} = \{\mathscr{R}\}_{n+1} &- \{\mathscr{C}\}\left[\mathbf{d}_n + (1-\gamma)\,\Delta t\,\ddot{\mathbf{d}}_n\right] \\
&- \{\mathscr{K}\}\left[\mathbf{d}_n + \Delta t\,\dot{\mathbf{d}}_n + \left(\frac{1}{2} - \beta\right)\Delta t^2 \ddot{\mathbf{d}}_n\right] \\
&- \{\mathscr{G}\}\left[\bar{\mathbf{d}}_n + \Delta t\,\mathbf{d}_n + \frac{\Delta t^2}{2}\dot{\mathbf{d}}_n + \left(\frac{1}{6} - \alpha\right)\Delta t^3 \ddot{\mathbf{d}}_n\right].
\end{aligned} \tag{64}$$

Equation (62) allows for the computation of the second-order terms at every $(n+1)$ time step; lower-order terms for the same time step are then recoverable via (59-61). In the applications that follow we used the average acceleration scheme.

5 Numerical Results

To test the accuracy of our mixed unsplit-field PML formulation, we discuss next two numerical experiments. The first pertains to a homogeneous half-space, whereas the second focuses on the effects of heterogeneity and involves a horizontally-layered system. For graphical presentation reasons, and without loss of generality, we have used low wave velocities to allow for clear wave front separation. In both simulations, we apply a distributed stress load on the surface, with a Ricker pulse time signature. The pulse is defined as

$$T_p(t) = \frac{(0.25u^2 - 0.5)e^{-0.25u^2} - 13e^{-13.5}}{0.5 + 13e^{-13.5}} \text{ for } u = \omega_r t - 3\sqrt{6}, \text{ and } 0 \le t \le \frac{6\sqrt{6}}{\omega_r}, \tag{65}$$

where ω_r is the characteristic Ricker central circular frequency $(= 2\pi f_r)$ of the pulse. Here, we used $f_r = 4$ Hz, and an amplitude of 10 Pa as depicted in Figure 3.

Beyond comparisons of time histories at select target locations, as a measure of PML performance, we provide plots of time-dependent error relative to a reference solution. To reproduce the semi-infinite extent of the unbounded domain on a computationally feasible scale, we compute (by using a displacement-based axisymmetric formulation) the response in an enlarged domain Ω^{ED} with fixed boundaries at a distance, such that the reflections from its fixed exterior boundaries do not travel back to the computational domain of interest Ω^{RD} within the specified time interval. We compare the responses only within the regular domain Ω^{RD} $(\subset \Omega^{ED})$. Introducing the time-dependent L^2 norm of the displacement field over a domain Ω as

$$D(t;\Omega) = \left[\int_{\Omega} \bar{\mathbf{v}}^T(\mathbf{x},t)\,\bar{\mathbf{v}}(\mathbf{x},t)\,\mathrm{d}\Omega\right]^{\frac{1}{2}}, \tag{66}$$
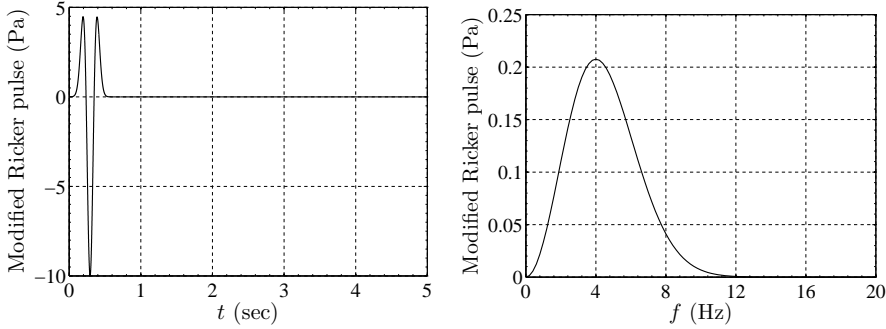
Figure 3: Ricker pulse time history and its Fourier spectrum

we define a relative error metric in terms of L^2 norms, normalized with respect to the peak value of the displacement field norm at all times within the regular domain region of the enlarged domain, as

$$e(t) = \frac{\left\{ \int_{\Omega^{\mathrm{RD}}} \left[\bar{\mathbf{v}}(\mathbf{x},t) - \bar{\mathbf{v}}_{\mathrm{ED}}(\mathbf{x},t) \right]^T \left[\bar{\mathbf{v}}(\mathbf{x},t) - \bar{\mathbf{v}}_{\mathrm{ED}}(\mathbf{x},t) \right] \, d\Omega^{\mathrm{RD}} \right\}^{\frac{1}{2}}}{\max D(t;\Omega^{\mathrm{ED}})} \times 100. \tag{67}$$

As an added metric of the PML's performance, we use the decay of the total energy within the regular domain, along lines similar to the ones discussed by Komatitsch and Martin (2007). The energy, injected to the domain via the loading, is carried by waves that are absorbed and attenuated within the PML, and, thus, decay should be expected if the PML is working properly. The total energy of the system as a function of time is expressed as

$$E_t(t) = \frac{1}{2} \int_{\Omega} \rho(\mathbf{x},t) \left[\mathbf{v}^T(\mathbf{x},t)\mathbf{v}(\mathbf{x},t) \right] d\Omega + \frac{1}{2} \int_{\Omega} \left[\sigma^T(\mathbf{x},t)\varepsilon(\mathbf{x},t) \right] d\Omega, \tag{68}$$

where $\mathbf{v}$, σ, and ε denote velocity, stress, and strain vectors, respectively. Again, the total energy is computed only within the regular domain Ω^{RD}.

5.1 *Homogeneous medium*

We considered a homogeneous half-space with density $\rho = 2200$ kg/m^3, shear wave velocity[3] $c_s \simeq 5.81$ m/s, and Poisson ratio $\nu = 0.2$. We truncated the semi-infinite extent of the original domain arriving at a 10m × 10m two-dimensional computational domain, through the introduction of a finite height (10m) cylindrical

---

[3] The low velocity is by design to allow for the ready wave pattern identification in plots; realistic velocities do not affect the quality of the results.
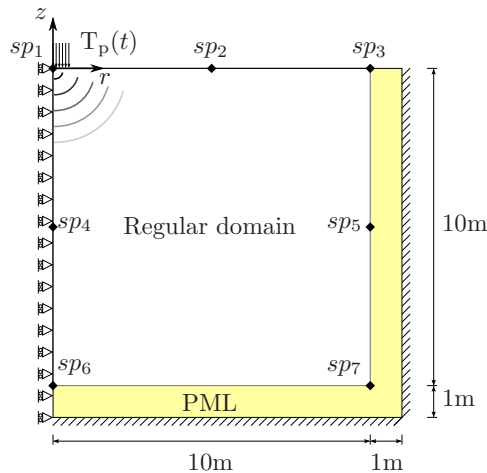
Figure 4: A PML-truncated axisymmetric domain subjected to a stress disk load on its surface over the region ($0\text{m} \leq r \leq 1\text{m}$)

surface of 10m radius. Surrounding the truncation surface is a 1m-thick PML, as shown in Figure 4; the PML wraps around the cylindrical truncation surface and extends also to the bottom of the computational domain. Symmetry boundary conditions were imposed along the axis of symmetry. Both the PML and the regular domain were discretized by quadratic quadrilateral elements with an element size of 0.1m. The mesh in the vicinity of the loading was refined by using 0.025m quadratic quadrilateral elements to properly resolve the local load effects. The discretization resulted in a 10-cell-thick PML. The reflection coefficient R was set to 10^{-8}. We used a time step of 0.002 seconds, and let the simulation run for 5 seconds. The time histories of the displacements (u_r, u_z), and stresses (σ_{rr}, $\sigma_{\theta\theta}$, σ_{zz}, σ_{rz}) are sampled at seven locations ($sp_i, i = 1 \ldots 7$), as shown in Figure 4.

The displacement time histories at the various sampling points were compared against the response obtained using an enlarged domain with fixed boundaries in lieu of the PMLs, and a classical displacement-based axisymmetric formulation. The enlarged domain's size (40m × 40m) was defined such that, during the specified time interval of interest (5 seconds), reflections from its fixed exterior boundaries do not travel back and interfere with the wave motion in the computational domain of interest. Figure 5 depicts the comparison of the response time histories for u_z at various sp_i points. As it can be seen the agreement is excellent. Moreover, no numerical instabilities were observed during the total simulation time that consisted of 2500 time steps.

Figure 6 depicts snapshots of u_z taken at two different times ($t = 1.35, 1.65$ sec) for
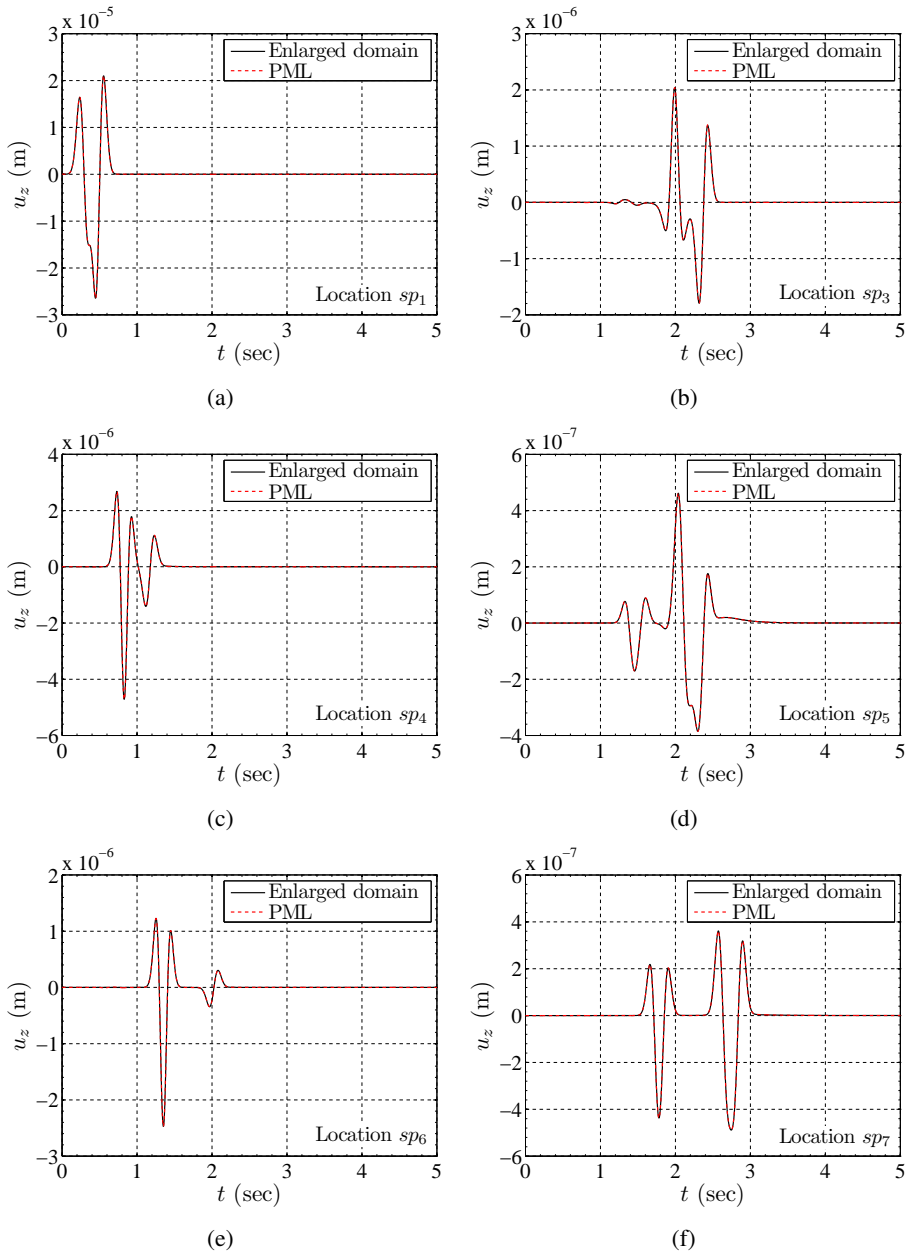
Figure 5: Time histories of u_z sampled within the regular domain and on the regular domain-PML interface

both the PML-truncated and the enlarged domain. The solid black lines in all the figures on the left column delineate the regular domain-PML interface. The right column figures depict snapshots taken of the enlarged domain simulations. Therein the dashed lines denote where the PML interface would have been (there is no PML in this case), in order to ease the comparison between the two sets of figures. Notice the excellent agreement (in the visual norm) of the two snapshot sets. Notice also the smoothness of the displacement contours along the regular domain-PML interface, betraying reflection-less PML behavior. Within the domain notice also the two distinct P- and S-wave trains: each wave train is marked by a tri-band, corresponding to the maxima and minima of the Ricker pulse. Figure 7 depicts snapshots (taken at two distinct times) of σ_{zz} for the PML-truncated domain; notice that there are no reflections from the interface.

Figure 8 shows the response time histories of u_z and σ_{zz} at a few sampling points. It is apparent from the figure that causality holds (sometimes a concern with PML implementations), and the response is free of spurious reflections. No numerical instabilities are observed.

Next, we illustrate the performance of the PML via the error metrics defined earlier. Figure 9 depicts the time-dependent displacement norm comparison and the normalized time-dependent relative error $e(t)$ in percent. The efficacy and quality of the PML is nicely corroborated by Figure 9(b) with a relative error that stays below 0.18% at all times.

To further test the quality of the obtained solutions, we record the energy within the regular domain as a function of time for different values of the reflection coefficient R, between $R = 10^{-1}$ and 10^{-8}. Figure 10 shows the energy decay plotted in standard (left), and semi-log scale (right). Shown on the same figure is a reference energy decay corresponding to the enlarged domain (recall that this has been obtained using an independent displacement-based formulation). There is a sharp ascent of the energy until about 0.4s, which corresponds to the highest peak of the Ricker pulse. By about $t = 1.05$s, the P-wave train has reached the bottom PML, with the first peak arriving at about $t = 1.25$s, and the major P-wave peak at about $t = 1.35$s. This is the point in time when the highest P-wave peaks reach the cylindrical truncation surface as well, and it is marked on the energy decay plot by the beginning of a sharp decline in the energy, as one would expect since the strongest wave motion has left the domain. By about $t = 2.02$s, the highest peak of the S-wave train has also reached the side and bottom PMLs (but not yet the domain corner), and also contributes to another sharp decline, as evidenced in the figure by a change in the slope. At, approximately, $t = 2.83$s the last S-wave peak has left the domain in the vicinity of the domain corner, and by about $t = 3$s all motion has seized within the domain –all of which are evident in the energy decay plot.

(a) u_z at $t = 1.35$ sec (PML)

(b) u_z at $t = 1.35$ sec (Enlarged domain)

(c) u_z at $t = 1.65$ sec (PML)
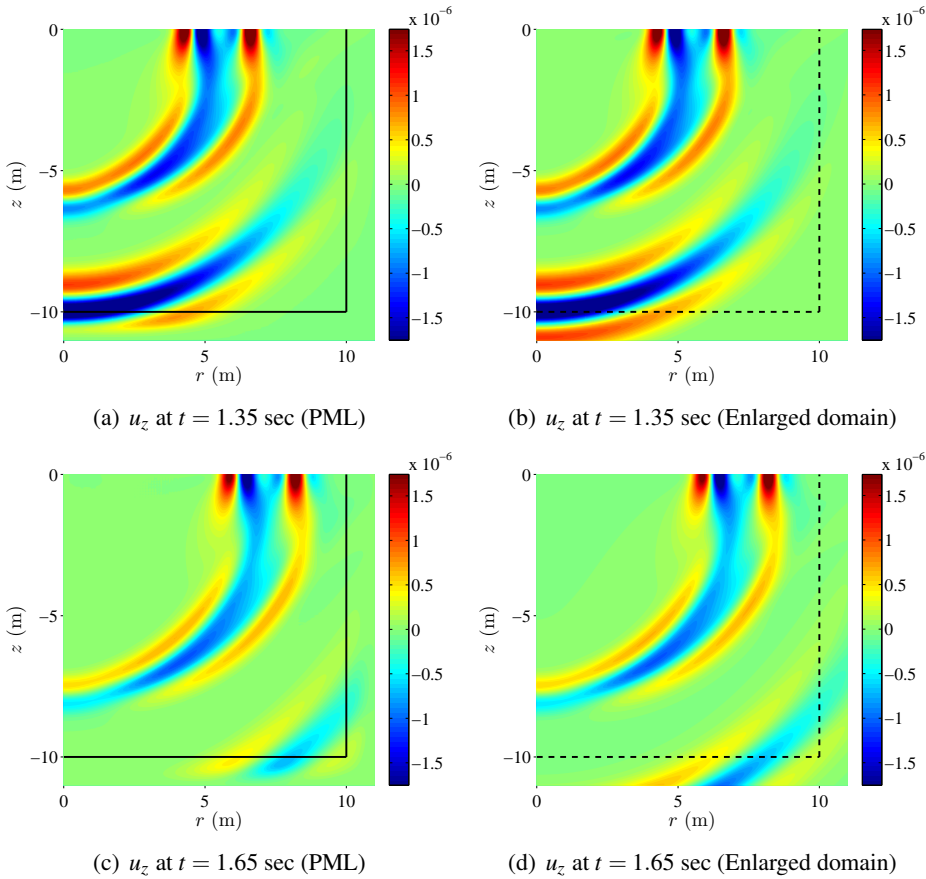
(d) u_z at $t = 1.65$ sec (Enlarged domain)

Figure 6: Comparison of u_z snapshots between the PML-truncated (left column) and enlarged (right column) domains - homogeneous medium

Notice further that for almost all R values (except for $R = 10^{-1}$) the performance of our new mixed PML formulation matches the enlarged domain's quite satisfactorily. A closer look, using the semi-log scale, reveals that lower R values enforce more rapid, and more accurate, decay, with R values less than about 10^{-6} driving the residual domain energy to about 10^{-8} or more than 5 orders of magnitude less than the peak domain energy.

Moreover, we let the simulation run for 40 seconds with a time step of 0.0002 seconds. As is evident from Figure 11, no numerical instabilities were observed during the total simulation time that consisted of 200,000 time steps.

(a) σ_{zz} at $t = 1.35$ sec $\qquad$ (b) σ_{zz} at $t = 1.65$ sec
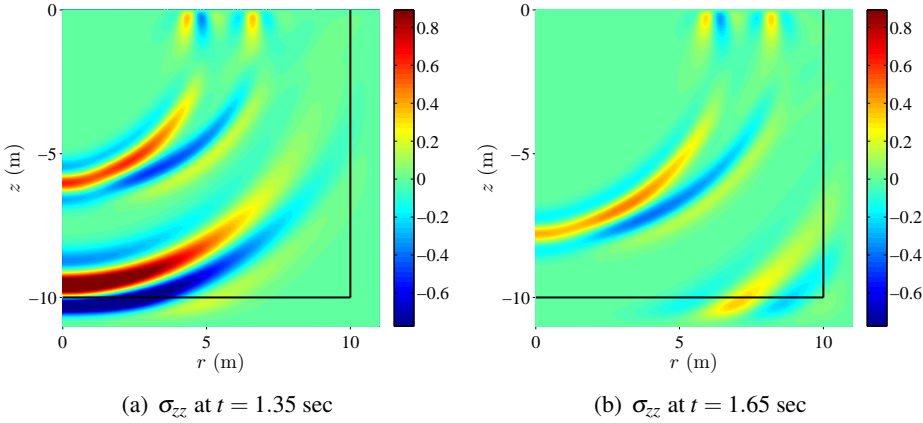
Figure 7: Snapshots of σ_{zz} for the PML-truncated domain - homogeneous medium

5.2 Heterogeneous medium

To illustrate the performance of PML in heterogeneous media, we consider a layered profile. Using a time step of 0.002 sec, we let the simulations run for 8 seconds. As shown in Figure 12, we considered a 5m × 5m layered medium, surrounded by 1m-thick PML on its cylindrical surface and bottom. We define

$$c_s(z) = \begin{cases} \sim 2.90 \text{ m/s}, & \text{for } -2\text{m} \leq z \leq 0\text{m}, \\ \sim 5.81 \text{ m/s}, & \text{for } -6\text{m} \leq z < -2\text{m}, \end{cases} \tag{69}$$

and the Poisson's ratio is again $\nu = 0.2$. The material interfaces were extended horizontally into the PML, thereby avoiding sudden material changes at the interface between the PML and the regular domain. The PML and the regular domain were discretized by quadratic quadrilateral elements with an element size of 0.1m, whereas in the vicinity of the surface load we used elements of size 0.025m. The reflection coefficient R was set to 10^{-8}, and we again simulated the wave motion using the PML formulation, as well as a displacement-based formulation for an enlarged domain with fixed exterior boundaries.

The displacement time histories at the various sampling points were compared against the response obtained using an enlarged domain (40m × 40m). The enlarged domain's size was defined such that, during the specified time interval of interest (8 seconds), reflections from its fixed exterior boundaries do not travel back and interfere with the wave motion in the computational domain of interest. Figure 13 depicts the comparison of the response time histories for u_z at various sp_i points. As it can be seen the agreement is impressive.
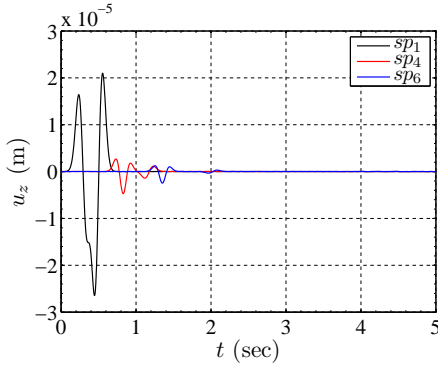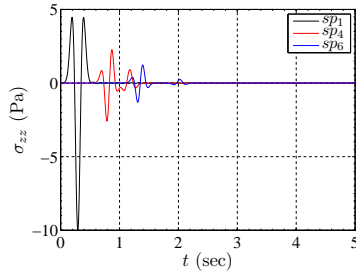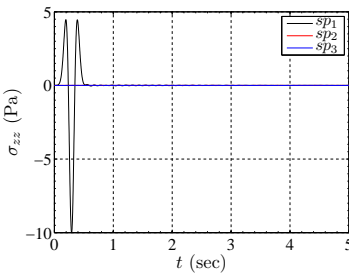
(a) u_z sampled at sp_1, sp_4, sp_6
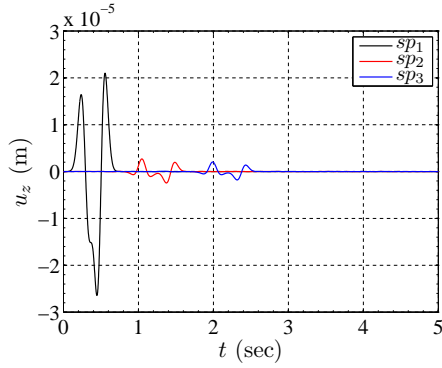
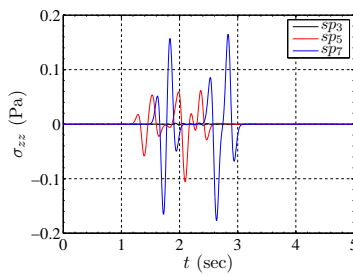(b) u_z sampled at sp_1, sp_2, sp_3
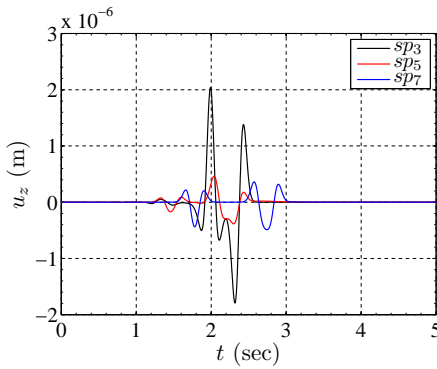
(c) u_z sampled at sp_3, sp_5, sp_7

(d) σ_{zz} sampled at sp_1, sp_4, sp_6

(e) σ_{zz} sampled at sp_1, sp_2, sp_3

(f) σ_{zz} sampled at sp_3, sp_5, sp_7

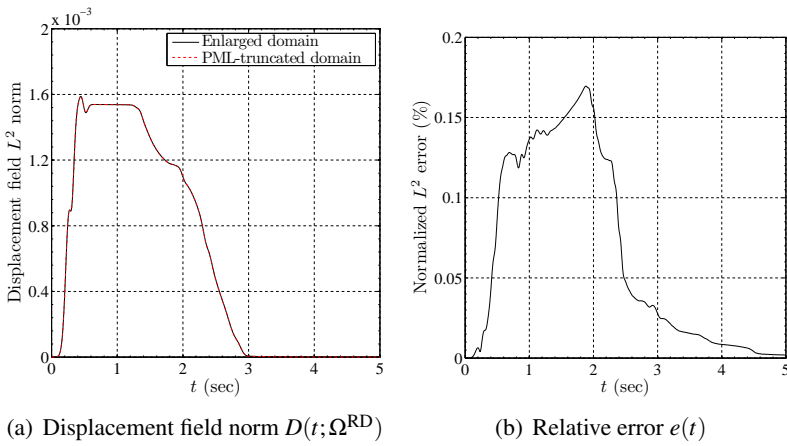Figure 8: Time histories of u_z and σ_{zz} at sampling points

(a) Displacement field norm $D(t; \Omega^{\mathrm{RD}})$ (b) Relative error $e(t)$

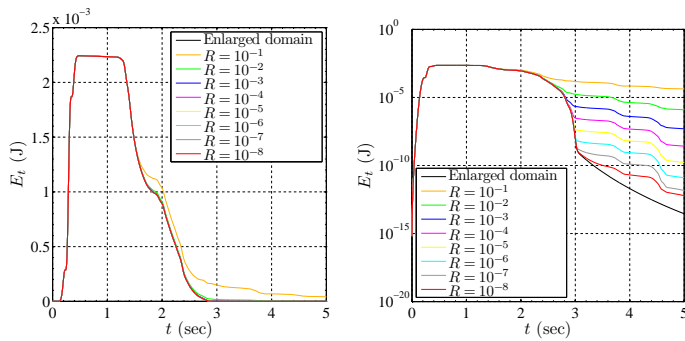Figure 9: Error metrics for the homogeneous domain (Example 1)

Figure 10: Total energy decay inside the regular domain - homogeneous medium
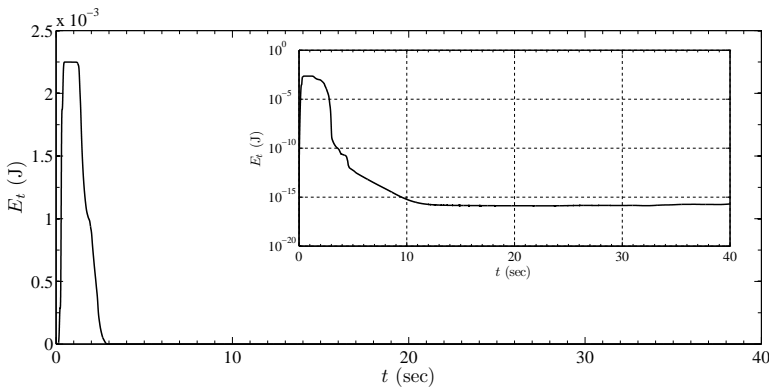

Figure 11: Long-time total energy decay inside the regular domain - homogeneous medium
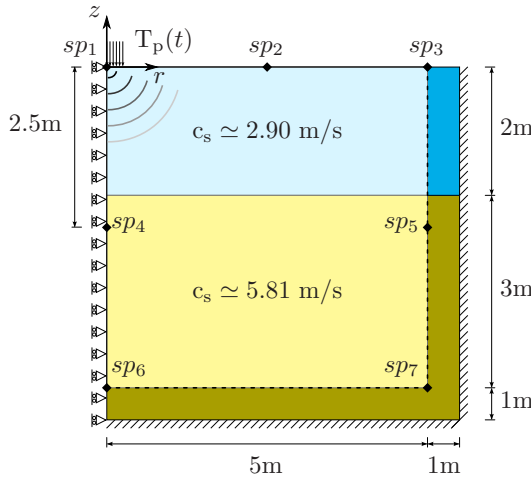
Figure 12: A PML-truncated axisymmetric domain subjected to a stress disk load on its surface over the region ($0\text{m} \le r \le 0.5\text{m}$)

Figure 14 shows the snapshots of displacement u_z taken at two different times ($t = 0.96\text{s}$ and 1.16s) for both the PML-truncated domain and the enlarged domain (40m $\times$ 40m). As before, we mark the PML-interface with dashed lines in the case of the enlarged domain to ease the visual comparison. The agreement is remarkable with no signs of instability or artificial reflections from the interface between the PML and regular domain. It is interesting to note that the waves are trapped inside the top layer due to the high-contrast ($1:2$) of the material properties of the two layers. The effect of the layer interface is clearly visible in the snapshots at $z = -2\text{m}$.

Next, we quantify the performance of the PML via the error metrics defined earlier. Figure 15 depicts the time-dependent displacement norm comparison and the normalized time-dependent relative error $e(t)$ in percent. The quality of the PML manifests itself with a nicely decaying relative error shown in Figure 15(b).

Lastly, Figure 16 depicts the energy decay within the layered medium: in this case the decay is considerably more gradual than in the homogeneous case, since there are multiple reflections off of the layer interface that travel back to the free surface, reflect at the free surface, travel downwards to the layer interface, partially reflect there, travel back to the free surface, and so on and so forth. We explored four different reflection coefficient values ($R = 10^{-2}, 10^{-4}, 10^{-6}$ and $R = 10^{-8}$). The observed behavior is similar to the one discussed in the case of the homogeneous host: overall, the PML performance is excellent, with no discernible reflections or instabilities, even in the presence of heterogeneity.
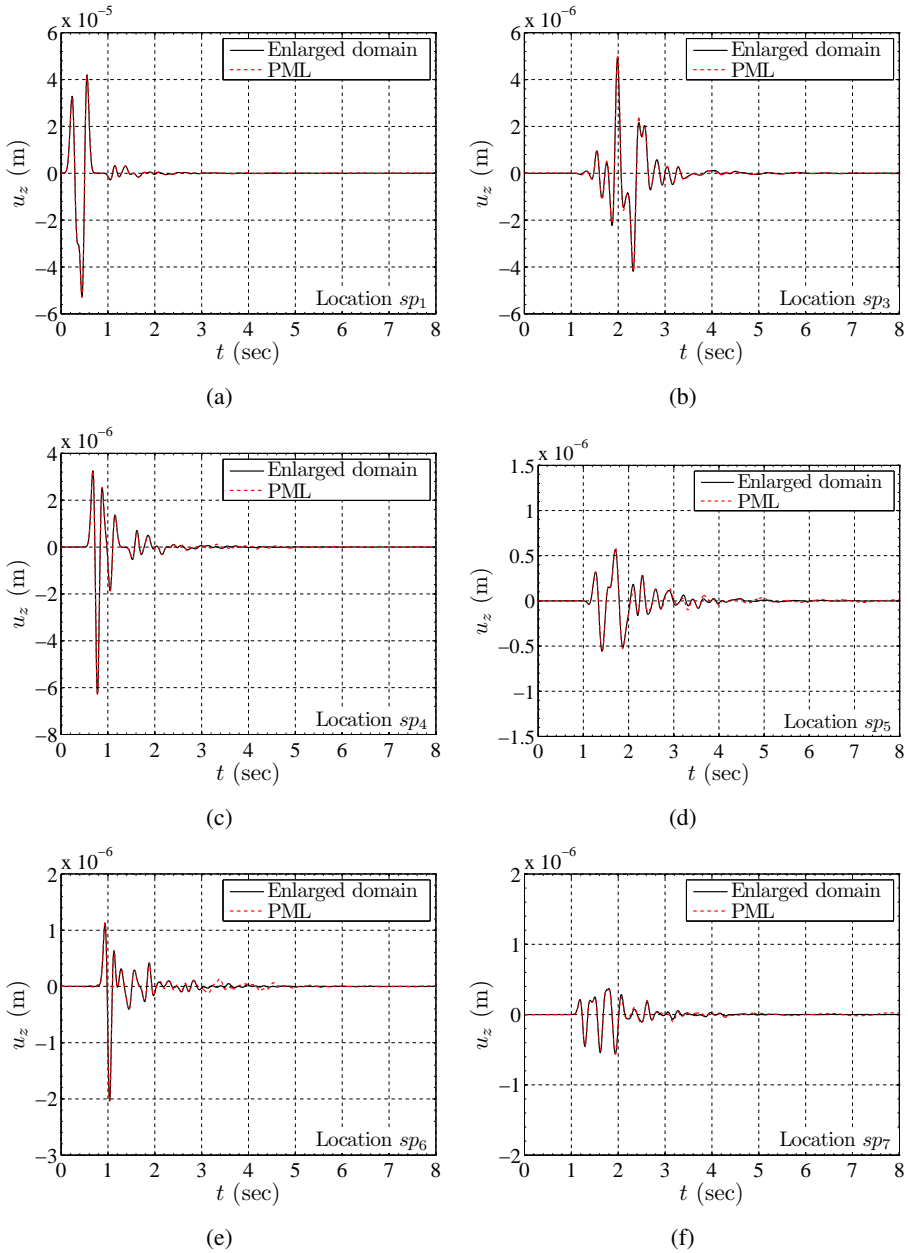
Figure 13: Time histories of u_z sampled within the regular domain and on the regular domain-PML interface

(a) u_z at $t = 0.96$ sec (PML)

(b) u_z at $t = 0.96$ sec (Enlarged domain)

(c) u_z at $t = 1.16$ sec (PML)
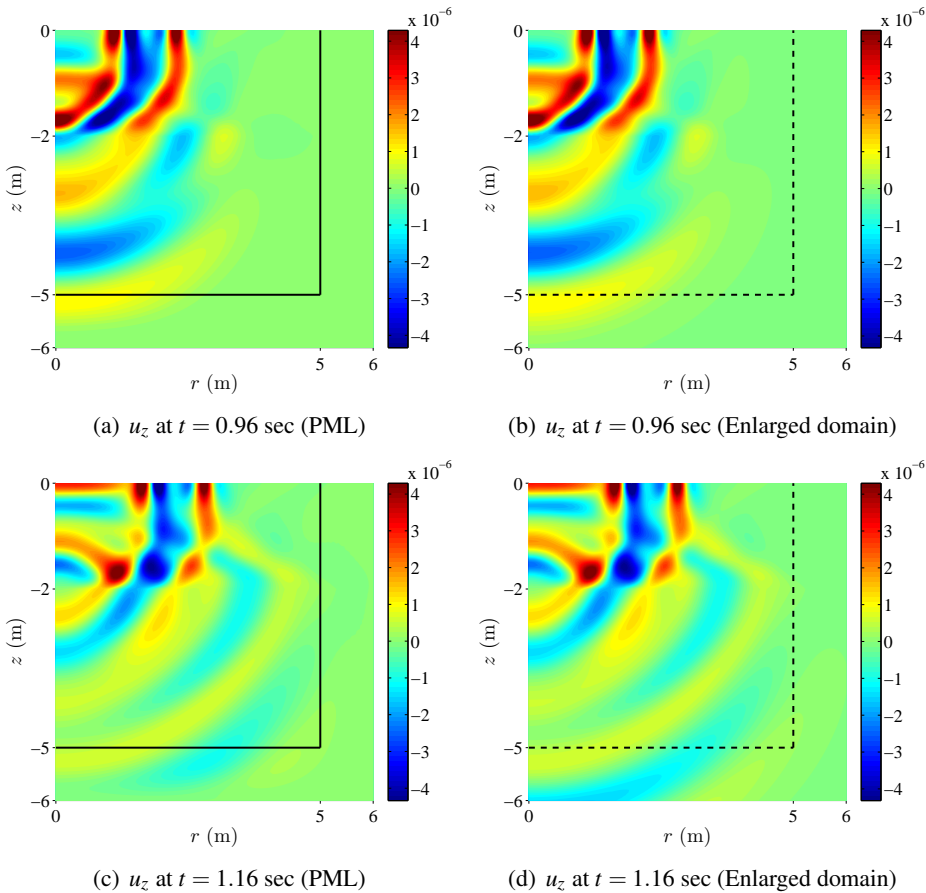
(d) u_z at $t = 1.16$ sec (Enlarged domain)

Figure 14: Comparison of u_z snapshots between the PML-truncated (left column) and enlarged (right column) domains - heterogeneous medium

We note that the efficacy of the discussed PML formulation does not depend on the complexity of the heterogeneity (e.g., multi-layered, non-horizontal layer interfaces, inclusions, etc). However, here we opted to report results for horizontally layered media only, since these are the most physically meaningful when axisymmetric geometries are considered.

Finally, we remark that growth of spurious reflections has been reported by others when waves impinge at grazing incidence at the PML-regular domain interface. It has also been often reported that the grazing incidence difficulty is associated with the choice of the classical stretching function, which, by construction, is singular at zero frequency (this has been our choice herein as well). To overcome the sin-

(a) Displacement field norm $D(t; \Omega^{RD})$ (b) Relative error $e(t)$
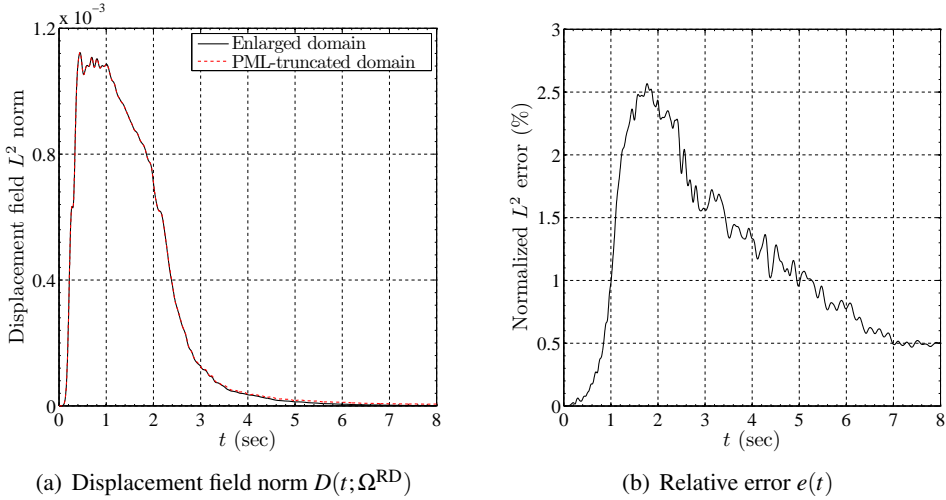
Figure 15: Error metrics for the heterogeneous domain (Example 2)

gularity, and possibly the perceived difficulty with the grazing angle incidence that has been attributed to the frequency singularity, modified stretching functions have been proposed that are not singular at zero frequency (as discussed in the introduction, the CPML is the most notable example of such a development: see, for example, Martin, Komatitsch, and Gedney (2008)). The CPML has been reported to alleviate, but not eliminate the growth of spurious reflections (see, for example, the comparisons reported in Meza-Fajardo and Papageorgiou (2008)). To date, all reported studies are purely numerical, and a theoretical proof of the origin of the difficulty remains elusive. It is not clear whether indeed the origin of the spurious growth at grazing incidence is due to the choice of the stretching function; moreover, careful parameterization of the PML is also capable of alleviating the growth. In this article, we too are not addressing the grazing angle incidence issue, pending detailed studies that escape the scope of this communication.

6 Conclusions

We presented the development of a new mixed displacement-stress (or stress history) formulation for forward elastic wave simulations in PML-truncated axisymmetric media. In particular, we used a regularly-stretched, unsplit-field PML, and retained both displacements and stress terms as unknowns to arrive at the mixed scheme. Upon the introduction of approximants, in the Galerkin sense, the resulting semi-discrete form can be cast as either third-order in time, or in an integro-
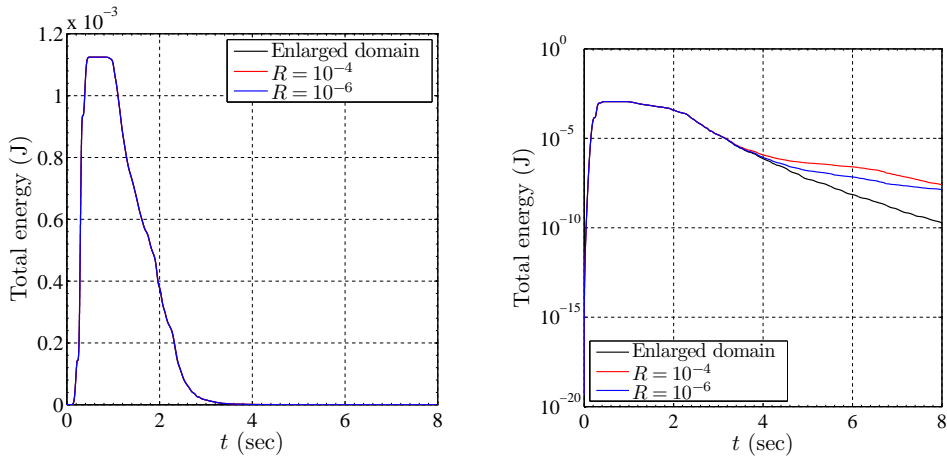
Figure 16: Total energy decay inside the regular domain - heterogeneous medium

differential form that includes second-order derivatives and a time-integral or memory-like term. We opted for the latter form, which, physically, implicates jerk terms for the displacements and stress-rate terms for the stresses, as the highest-order derivatives present. We discussed an extended Newmark-β scheme for integrating in time the semi-discrete forms.

Although the choice of a mixed method increases the number of unknowns, when compared against a displacement-only formulation (which does not exist for the problem at hand), it compares quite favorably against split-field mixed approaches.

We reported numerical experiments demonstrating excellent agreement against reference numerical solutions, as well as excellent PML absorption abilities. We have observed no instabilities, or non-causal behavior. We remark that for stability, as in all mixed problems, the choice of the approximants cannot be arbitrary (Xue, Karlovitz, and Atluri (1985)), but must satisfy an *inf-sup* condition (also referred to as Ladyzhenskaya-Babuška-Brezzi (LBB) condition). With respect to the approximants, we have found both bilinear-bilinear and biquadratic-biquadratic pairs of approximants to be *numerically* stable (we reported simulations only with the biquadratic pair).

As is known, the discretization of the PML introduces inevitably the mesh density as a parameter. For the absorption to be effective, it is critical that the mesh density within the PML adequately captures the imposed decay profile. A sharp decay necessitates more elements within the PML, and, in our experience, the PML's mesh density plays a critical role in the generation of spurious wave motion, especially in the presence of waves impinging at grazing or near-grazing angle upon the PML

interface. Although there exists an optimal set of PML parameters (amplitude and power of decay polynomial) for a given mesh density[4], we have found that, in general, one could expect reasonable performance by using a quadratic profile and a reference velocity equal to the average P-wave velocity of the computational domain.

The extension of the methodology reported herein to the three-dimensional case is straightforward, and will be reported in future communications. While not addressed herein, the choice of the PML parameters (reference velocity, mesh density, reflection coefficient, etc) is critical in presenting the wave motion with a smoothly-varying decay profile within the PML. A relatively smooth profile is necessary for avoiding spurious reflections that could pollute the solution in the interior. A thorough parametric study escapes the scope of the present article, but is necessary for providing guidance on the parameter choices, and, in turn, for quality solutions.

References

Arnold, D. N.; Brezzi, F.; Douglas, J. (1984): PEERS: a new mixed finite element for plane elasticity. *Japan J. Appl. Math*, vol. 1, pp. 347–367.

Arnold, D. N.; Brezzi, F.; Fortin, M. (1984): A stable finite element for the stokes equations. *Calcolo*, vol. 21, pp. 337–344.

Atluri, S. N.; Gallagher, R. H.; Zienkiewicz, O. C. (1983): *Hybrid & mixed finite element methods*. J. Wiley & Sons, Chichester.

Basu, U. (2009): Explicit finite element perfectly matched layer for transient three-dimensional elastic waves. *Int. J. Numer. Meth. Engng.*, vol. 77, pp. 151–176.

Basu, U.; Chopra, A. K. (2003): Perfectly matched layers for time-harmonic elastodynamics of unbounded domains: theory and finite-element implementation. *Comput. Methods Appl. Mech. Engrg.*, vol. 192, pp. 1337–1375.

Basu, U.; Chopra, A. K. (2004): Perfectly matched layers for transient elastodynamics of unbounded domains. *Int. J. Numer. Meth. Engng.*, vol. 59, pp. 1039–1074.

---

[4] There is no simple process that could lead *a priori* to an optimal set of PML parameters; an optimization-based process has been reported in Collino and Monk (1998).

Bécache, E.; Fauqueux, S.; Joly, P. (2003):   Stability of perfectly matched layers, group velocities and anisotropic waves.   *Journal of Computational Physics*, vol. 188, pp. 399–433.

Bécache, E.; Joly, P.; Tsogka, C. (2001):   Fictitious domains, mixed finite elements and perfectly matched layers for 2D elastic wave propagation.   *J. Comput. Acoust.*, vol. 9, no. 3, pp. 1175–1202.

Bérenger, J.-P. (1994):   A perfectly matched layer for the absorption of electromagnetic waves.   *Journal of Computational Physics*, vol. 114, pp. 185–200.

Bérenger, J.-P. (2002):   Application of the CFS PML to the absorption of evanescent waves in waveguides.   *IEEE Microwave and Wireless Components Letters*, vol. 12, no. 6, pp. 218–220.

Bérenger, J.-P. (2002):   Numerical reflection from FDTD-PMLs: a comparison of the split PML with the unsplit and CFS PMLs.   *IEEE Transactions on Antennas and Propagation*, vol. 50, no. 3, pp. 258–265.

Brezzi, F. (1988):   A survey of mixed finite element method. In Dwoyer, D.; Hussaini, M.; Voigt, R.(Eds):   *Finite Elements Theory and Application*, pp. 34–49, New York. Springer-Verlag.

Brezzi, F.; Douglas, J.; Marini, L. D. (1985):   Two families of mixed finite element methods for second order elliptic problems.   *Numer. Math.*, vol. 47, pp. 217–235.

Chew, W. C.; Jin, J. M.; Michielssen, E. (1997):   Complex coordinate system as a generalized absorbing boundary condition. In *Proc. 13th Annu. Rev. of Prog. Appl. Comp. Electromag.*, pp. 909–914, Monterey,CA. Vol. 2.

Chew, W. C.; Liu, Q. H. (1996):   Perfectly matched layers for elastodynamics: a new absorbing boundary condition.   *Journal of Computational Acoustics*, vol. 4, no. 4, pp. 341–359.

Chew, W. C.; Weedon, W. H. (1994):   A 3D perfectly matched medium from modified Maxwell's equations with stretched coordinates.   *Micro. Opt. Tech. Lett.*, vol. 7, pp. 599–604.

Cohen, G.; Fauqueux, S. (2005):   Mixed spectral finite elements for the linear elasticity system in unbounded domains.   *SIAM J. Sci. Comput.*, vol. 26, no. 3, pp. 864–884.

Collino, F.; Monk, P. B. (1998):   Optimizing the perfectly matched layer.   *Comput. Methods Appl. Mech. Engrg.*, vol. 164, pp. 157–171.

Collino, F.; Tsogka, C. (2001): Application of the perfectly matched absorbing layer model to the linear elastodynamic problem in anisotropic heterogeneous media. *Geophysics*, vol. 66, no. 1, pp. 294–307.

Drossaert, F. H.; Giannopoulos, A. (2007): Complex frequency shifted convolution PML for FDTD modelling of elastic waves. *Wave Motion*, vol. 44, no. 7-8, pp. 593–604.

Drossaert, F. H.; Giannopoulos, A. (2007): A nonsplit complex frequency-shifted PML based on recursive integration for FDTD modeling of elastic waves. *Geophysics*, vol. 72, no. 2, pp. T9–T17.

Farrell, C.; Leonhardt, U. (2005): The perfectly matched layer in numerical simulations of nonlinear and matter waves. *Journal of Optics B: Quantum and Semiclassical Optics*, vol. 7, pp. 1–4.

Festa, G.; Nielsen, S. (2003): PML absorbing boundaries. *Bulletin of the Seismological Society of America*, vol. 93, no. 2, pp. 891–903.

Festa, G.; Vilotte, J.-P. (2005): The Newmark scheme as velocity-stress time-staggering: an efficient PML implementation for spectral element simulations of elastodynamics. *Geophys. J. Int.*, vol. 161, pp. 789–812.

Gedney, S. D. (1996): An anisotropic perfectly matched layer-absorbing medium for the truncation of FDTD lattices. *IEEE Transactions on Antennas and Propagation*, vol. 44, no. 12, pp. 1630–1639.

Harari, I.; Albocher, U. (2006): Studies of FE/PML for exterior problems of time-harmonic elastic waves. *Comput. Methods Appl. Mech. Engrg.*, vol. 195, pp. 3854–3879.

Hastings, F. D.; Schneider, J. B.; Broschat, S. L. (1996): Application of the perfectly matched layer (PML) absorbing boundary condition to elastic wave propagation. *J. Acoust. Soc. Am.*, vol. 100, no. 5, pp. 3061–3069.

Hu, F. Q. (1996): On absorbing boundary conditions for linearized Euler equations by a perfectly matched layer. *Journal of Computational Physics*, vol. 129, pp. 201–219.

Johnson, C.; Mercier, B. (1978): Some equilibrium finite element methods for two-dimensional elasticity problems. *Numer. Math.*, vol. 30, pp. 103–116.

Komatitsch, D.; Martin, R. (2007): An unsplit convolutional perfectly matched layer improved at grazing incidence for the seismic wave equation. *Geophysics*, vol. 72, no. 5, pp. SM155–SM167.

Komatitsch, D.; Tromp, J. (2003):   A perfectly matched layer absorbing boundary condition for the second-order seismic wave equation.   *Geophysical Journal International*, vol. 154, pp. 146–153.

Kuzuoglu, M.; Mittra, R. (1996):   Frequency dependence of the constitutive parameters of causal perfectly matched anisotropic absorbers.   *IEEE Microwave and Guided Wave Letters*, vol. 6, no. 12, pp. 447–449.

Liu, Q. H. (1999):   Perfectly matched layers for elastic waves in cylindrical and spherical coordinates.   *J. Acoust. Soc. Am.*, vol. 105, no. 4, pp. 2075–2084.

Liu, Q. H.; He, J. Q. (1998):   Quasi-PML for waves in cylindrical coordinates. *Microwave and Optical Technology Letters*, vol. 19, no. 2, pp. 107–111.

Liu, Q. H.; Sinha, B. K. (2003):   A 3D cylindrical PML/FDTD method for elastic waves in fluid-filled pressurized boreholes in triaxially stressed formations. *Geophysics*, vol. 68, no. 5, pp. 1731–1743.

Martin, R.; Komatitsch, D.; Gedney, S. (2008):   A variational formulation of a stabilized unsplit convolutional perfectly matched layer for the isotropic or anisotropic seismic wave equation. *CMES: Computer Modeling in Engineering & Sciences*, vol. 37, no. 3, pp. 274–304.

Meza-Fajardo, K. C.; Papageorgiou, A. S. (2008):   A nonconvolutional, split-field, perfectly matched layer for wave propagation in isotropic and anisotropic elastic media: Stability analysis. *Bulletin of the Seismological Society of America*, vol. 98, no. 4, pp. 1811–1836.

Raviart, P. A.; Thomas, J. M. (1977):   A mixed finite element method for second order elliptic problems. In Galligani, I.; Magenes, E.(Eds): *Mathematical Aspects of the Finite Element Method, Lecture Notes in Mathematics*, volume 606, pp. 292–315, New York. Springer-Verlag.

Roden, J. A.; Gedney, S. D. (2000):   Convolutional PML (CPML): an efficient FDTD implementation of the CFS-PML for arbitrary media. *Microwave and Optical Technology Letters*, vol. 27, no. 5, pp. 334–339.

Roden, J. A.; Gedney, S. D. (2000):   An efficient FDTD implementation of the PML with CFS in general media. *IEEE Antennas and Propagation Society International Symposium*, vol. 3, pp. 1362–1265.

Teixeira, F. L.; Chew, W. C. (1997):   Perfectly matched layer in cylindrical coordinates. In *Antennas and Propagation Society International Symposium Digest*, pp. 1908–1911, Montreal, Canada. IEEE. Vol. 3.

Teixeira, F. L.; Chew, W. C. (1997):   PML-FDTD in cylindrical and spherical grids. *IEEE Microwave and Guided Wave Letters*, vol. 7, no. 9, pp. 285–287.

Teixeira, F. L.; Chew, W. C. (1997): Systematic derivation of anisotropic PML absorbing media in cylindrical and spherical coordinates. *IEEE Microwave and Guided Wave Letters*, vol. 7, no. 11, pp. 371–373.

Teixeira, F. L.; Chew, W. C. (1999): On causality and dynamic stability of perfectly matched layers for FDTD simulations. *IEEE Transactions on Microwave Theory and Techniques*, vol. 47, no. 6, pp. 775–785.

Teixeira, F. L.; Chew, W. C. (2000): Complex space approach to perfectly matched layers: a review and some new developments. *Int. J. Numer. Model.*, vol. 13, pp. 441–455.

Tsynkov, S. V. (1998): Numerical solution of problems on unbounded domains. a review. *Appl. Numer. Math.*, vol. 27, no. 4, pp. 465–532.

Turkel, E.; Yefet, A. (1998): Absorbing PML boundary layers for wave-like equations. *Applied Numerical Mathematics*, vol. 27, pp. 533–557.

Wang, J.; Wang, Y.; Zhang, D. (2006): Truncation of open boundaries of cylindrical waveguides in 2.5-dimensional problems by using the convolutional perfectly matched layer. *IEEE Transactions on Plasma Science*, vol. 34, no. 3, pp. 681–690.

Wang, T.; Tang, X. (2003): Finite-difference modeling of elastic wave propagation: A nonsplitting perfectly matched layer approach. *Geophysics*, vol. 68, no. 5, pp. 1749–1755.

Xue, W.-M.; Karlovitz, L. A.; Atluri, S. N. (1985): On the existence and stability conditions for mixed-hybrid finite element solutions based on reissner's variational principle. *J. of Solids and Structures*, vol. 21, no. 1, pp. 97–116.

Zampolli, M.; Tesei, A.; Jensen, F. B. (2007): A computationally efficient finite element model with perfectly matched layers applied to scattering from axially symmetric objects. *J. Acoust. Soc. Am.*, vol. 122, no. 3, pp. 1472–1485.

Zeng, Y.; He, J. Q.; Liu, Q. H. (2001): The application of the perfectly matched layer in numerical modeling of wave propagation in poroelastic media. *Geophysics*, vol. 66, no. 4, pp. 1258–1266.

Zhao, L. (2000): The generalized theory of perfectly matched layers (GT-PML) in curvilinear co-ordinates. *Int. J. Numer. Model.*, vol. 13, pp. 457–469.